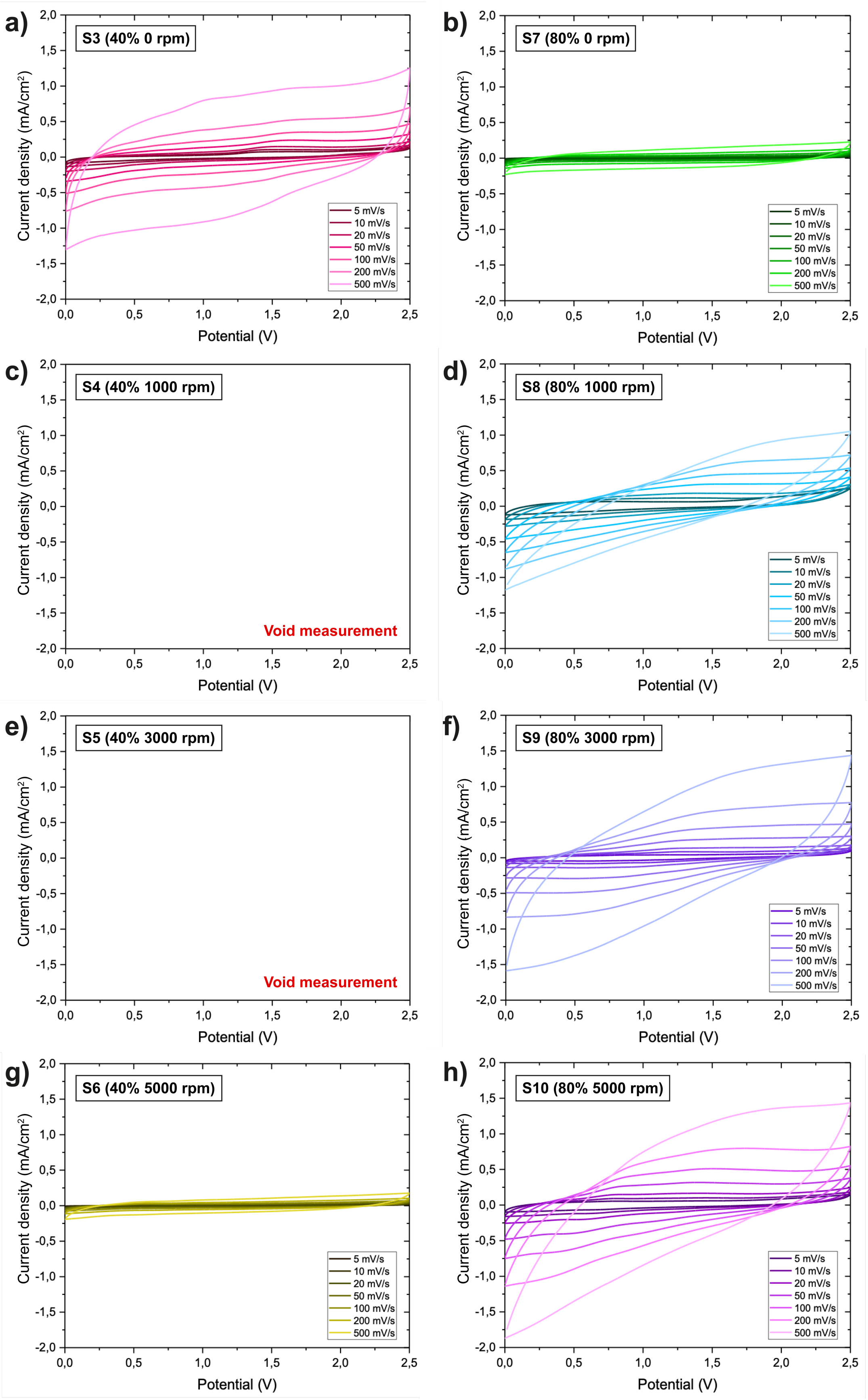

Figure 47: CV comparison between all LIG MSCs with MoS_2 at different conditions

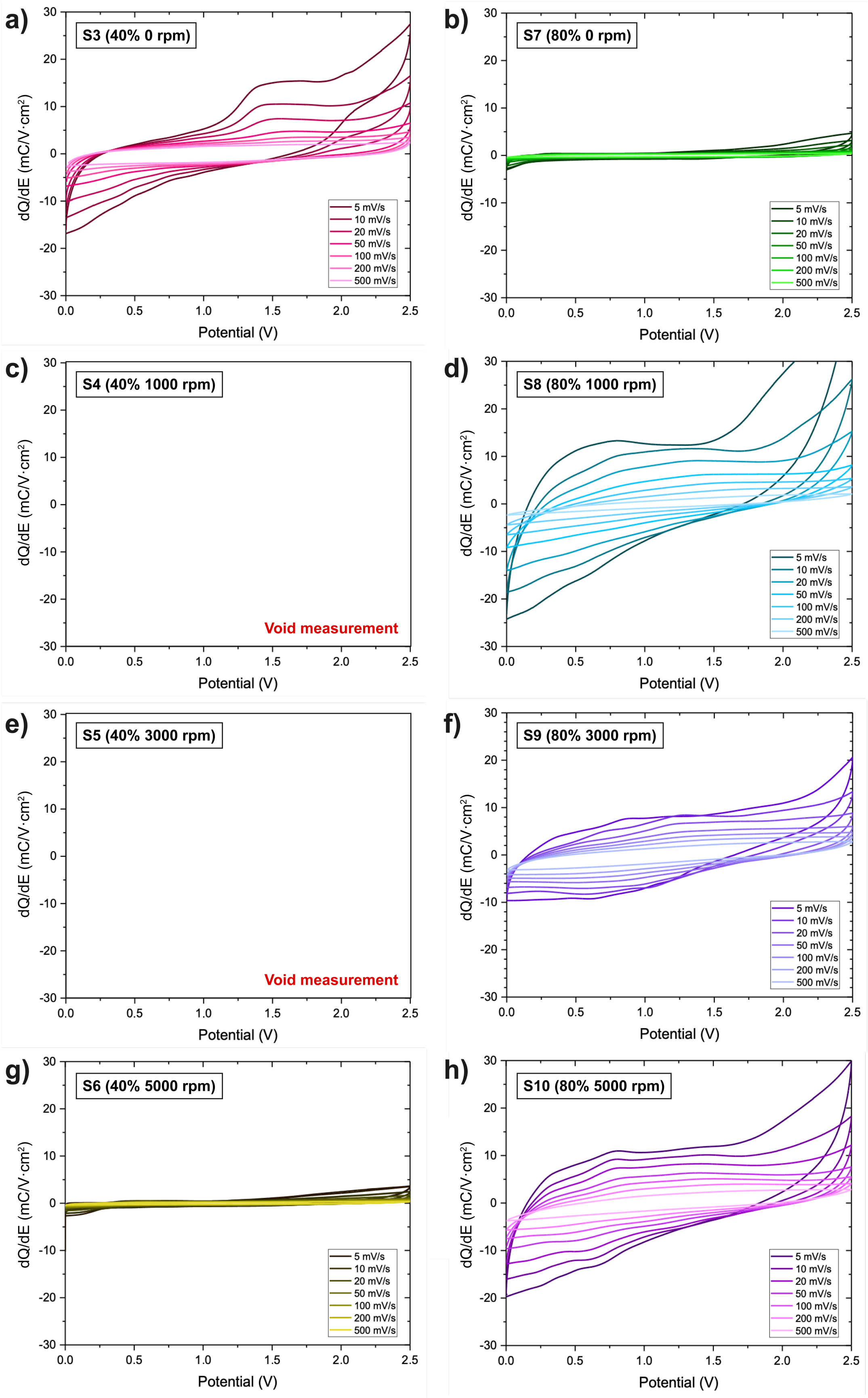

Figure 48: dQ/dE CV comparison between all LIG MSCs with MoS_2 at different conditions.

In Figure 47 and Figure 48, the CV and dQ/dE measurements of all eight samples are shown at the same scale. A few observations can be made directly. Devices 80_0 and 40_5000 show a very small current in comparison to the other devices, only comparable to devices S1 and S2 made in December. All eight samples, S3 to S10, were made under the same conditions, so this low performance could be attributed to damaging of the LIG substrate during manual handling, or to a bad contact during sample fabrication. This variation makes it complicated to extract conclusions in the 80% EtOH series. For the 40% series, samples 40_3000 and 40_5000 could not be plotted due to inconsistencies during measurement.

The Electrochemical Impedance Spectroscopy data (see Figure 49) shows a big variability in the measured impedance between all samples, which also translates to the measured Rs parameter for each device. This parameter, as explained before, is extracted as the cross with the x-axis of the Nyquist plot, so an inset with a zoomed region of the graph is placed alongside the full one.

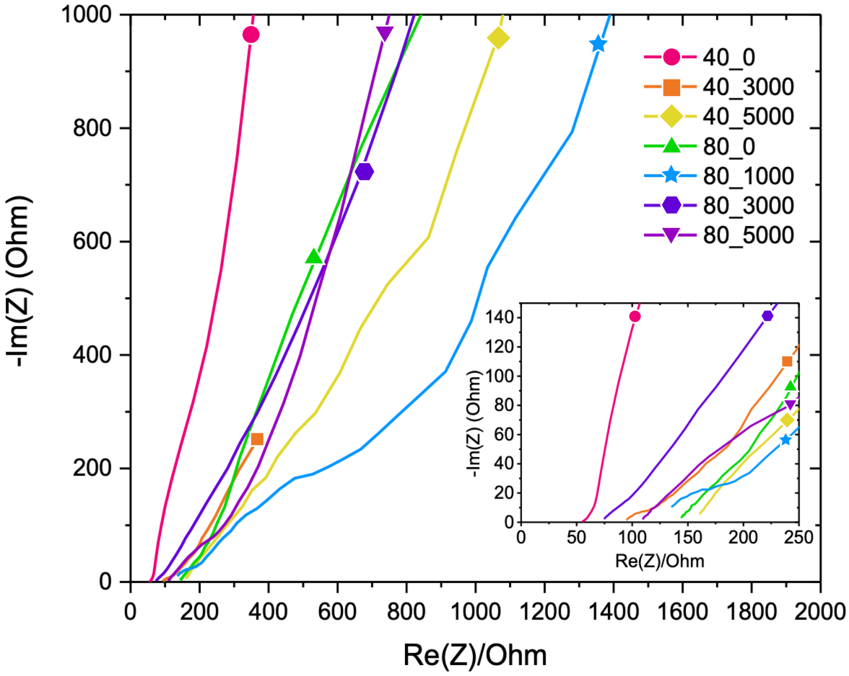

Figure 49: Electrochemical Impedance Spectroscopy data of all samples. Inset: zoomed region to visualize clearly the cross with the x-axis.

Furthermore, the results were confirmed by extracting the ERS value from the galvanostatic charge-discharge characterization, using equation 2.4, plotted in Figure 50. Both measurements show the same trend, and the difference between them is easily explained, as the solid columns' data are extracted from the EIS measurement, this represents the electrode resistance. On the other hand, the more transparent columns represent the ESR value extracted from GCD measurements, which represents more resistance factors, including the electrolyte and its interfaces. In any case, both measurements show similar results, as 40_0 (S3) is the lowest resistive device, while 40_5000 (S6) is the highest.

By further analysis of the GCD data, using a custom python code, the areal capacitance for each device can be extracted. This data is plotted in Figure 51 showing the capacitance variation with the current density. In Figure 51b, the capacitance data is normalized by the highest capacitance value for each sample.

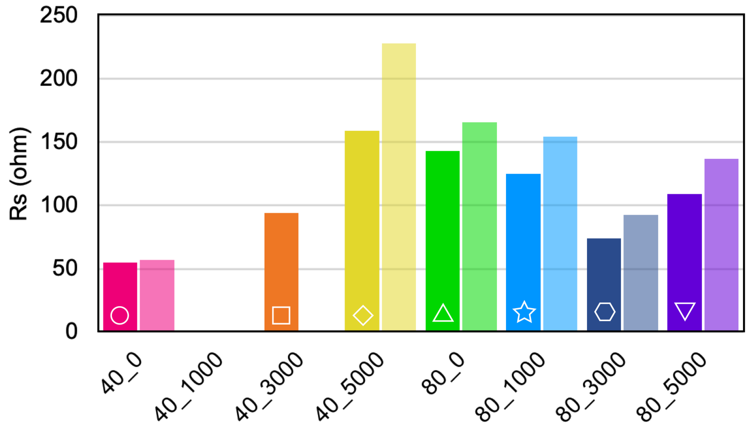

Figure 50: Series resistance values plot for all MoS_2 LIG devices. In solid, the Rs values extracted from EIS measurements. Transparent columns (right) represent the equivalent series resistance (ESR) extracted from galvanostatic charge-discharge measurements.

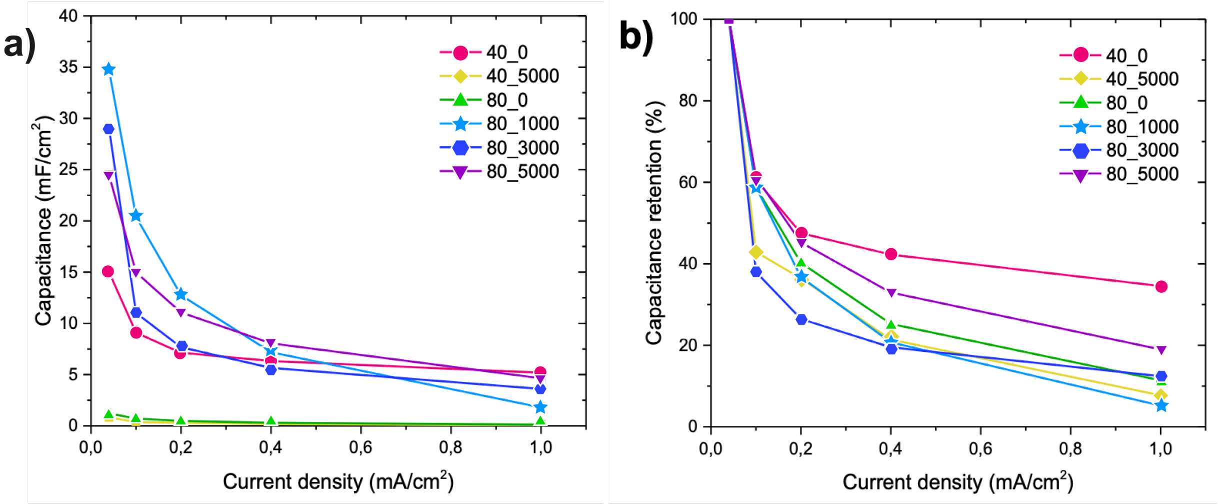

Figure 51: Comparison of the capacitance of the MoS_2 LIG microsupercapacitors. Areal capacitance vs current density for all devices. Calculated from GCD measurements using a custom python code. (b) Plot showing the capacitance retention with increasing current density. Capacitance values from GCD, normalized by the capacitance at 0.04 mA/cm² for each sample.

For the six devices that could be fully characterized, we observe that the samples having the lowest series resistance are the ones that keep better the capacitance at high current densities, such as 40_0 (the “flattest”) and to a lesser extent 80_3000 and 80_5000. Regarding the best performance at low current densities, we get promising results, with 80_1000 showing capacitances of almost 35 mF/cm^2 at 0.04 mA/cm^2, although its higher resistance is responsible for the quicker drop of the capacitance at high currents.

To better observe this behaviour, Figure 51b shows the same data, normalized for each device to the capacitance at 0.04 mA/cm^2 (100%) to analyze the capacitance retention with increasing current density. It can be observed that 40_0, the less resistive sample, is the one that shows the highest retention, of around 40% at 1 mA/cm^2. 80_3000 shows an abnormally high capacitance at the lowest current, which falls towards a lower value, which is kept for high currents as expected, as its resistance is also very low. 80_5000 is the best sample overall, with a high capacitance value at low currents and a decent capacitance retention at 1mA/cm^2.

The most used comparison plot to study supercapacitors is the Ragone plot, where the measured devices are compared in terms of its areal energy density and areal power density. Figure 52 shows this plot for the six samples that could be fully characterized. In this plot, we observe similar results to those in Figure 51a. Samples 40_5000 and 80_0 are out of range, with much worse performance than the rest. For the other four samples, the same trends can be seen, with 40_0 having the best energy density at high powers, and the worst at low powers. 80_5000 is again showing a good overall performance, with good energy density at both extremes of the plot.

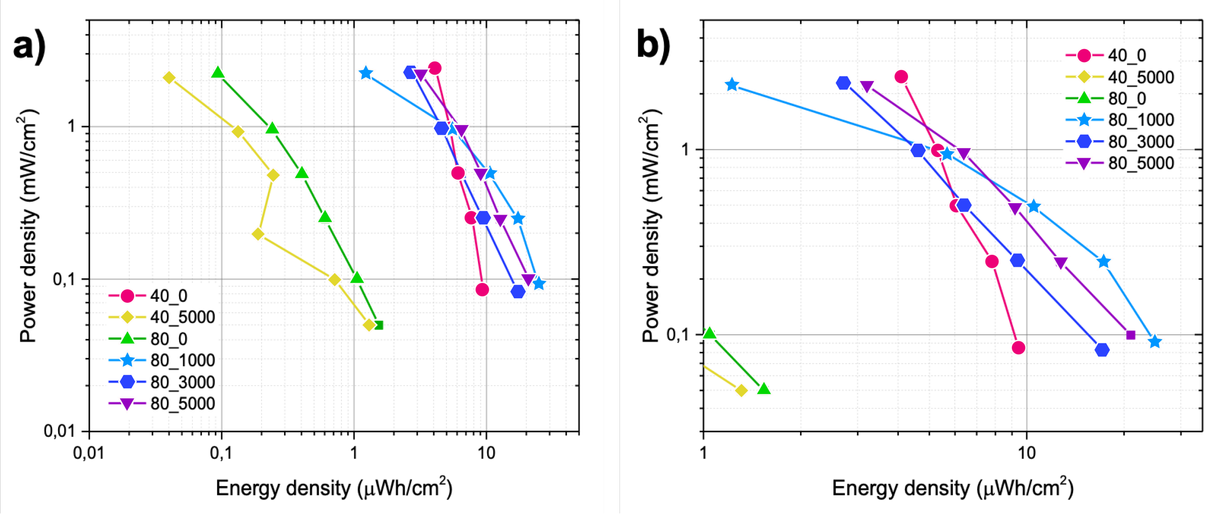

Figure 52: Ragone plot of the MoS$_2$ LIG MSCs. (a) Ragone plot of the measured devices. (b) Zoomed region showing only the best four devices.

The energy densities range between 10 and 25 µWh/cm² for low current densities of 0.04 mA/cm² or 0.1 mW/cm², and between 1.22 and 4.13 µWh/cm² for a maximum power density of 2.25 mW/cm², at a current of 1 mA/cm².

It is interesting to contextualize these values with other LIG devices, in order to clarify if the use of MoS_2 and its oxides brings any real improvement. To do this, future work is needed as the amount of samples that could be measured has been very limited. However, a theoretical approximation can be performed. This comparison is made against the best device presented in section 4.2.2, S-2.0-45, which Ragone plot is replicated in red circles in Figure 53a.

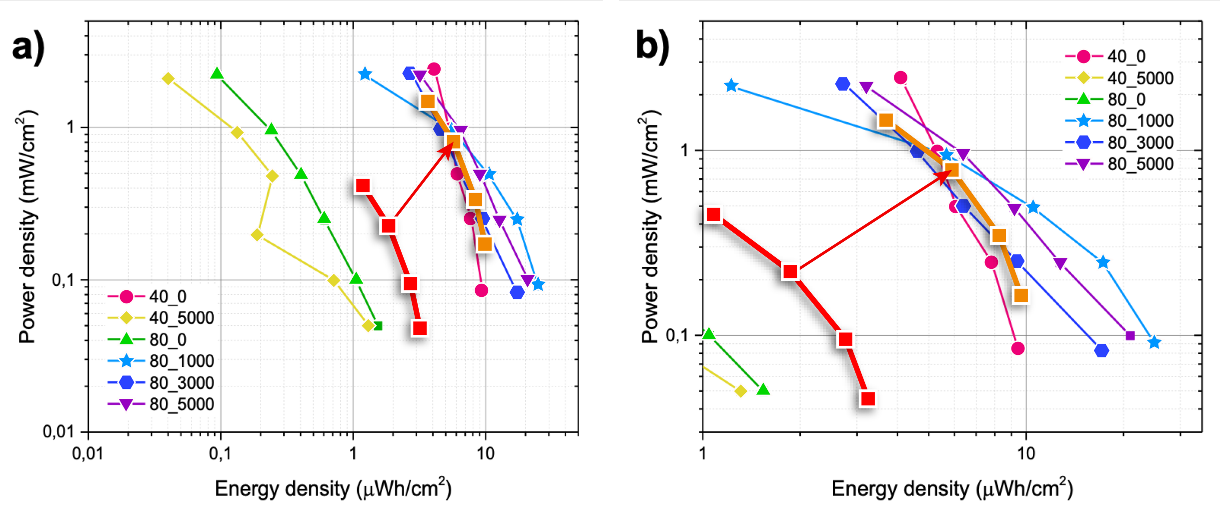

Figure 53: Theoretical comparison of LIG MSCs hypothetically measured in ionic liquid, with the MoS_2 LIG MSCs fabricated. (a) Ragone plot of the devices complemented with MoS2, together with two extra devices. In red circles, S-2.0-45 taken from section 4.1, and in orange triangles the same data, theoretically translated to take into account the change in conditions. (b) Same plot, zoomed to show better the region of interest.

To make this theoretical translation of the values, a rude first approximation be made using equations 2.3 and 2.4, presented in section 2. The energy density, according to equation 2.3, depends on the capacitance of the device, and on the square of the voltage window. For the voltage window, an increase from 1 V to 2.5 V would yield an energy density increase of 6.25x. However, the capacitance is theoretically reduced, some studies suggest that due to the difference in ion size, higher viscosity and lower conductivity of the electrolyte, capacitance can be expected to be approximately reduced by half, 0.5x [198]. In the same way, power density can be expected to increase the same factor than the energy density.

By applying these conversion factors, the energy density and power density data of S-2.0-45 could be modified, to show a tentative performance if the sample was measured in ionic liquid electrolyte on an extended voltage window. This result shows the potential improvement that compositing with molybdenum oxides bring, taken into account the many unknowns that this study still has. The energy density can reach values that more than double the expected ones for bare LIG, while the power density is slightly improved as well.

However, this rude approximation does not consider the change in properties brought by the use of a different LIG material, double pass with high laser power. Furthermore, more experiments are needed in order to extract more conclusions, as only one device has been fabricated for each MoS_2 condition, and many samples offered resistivities that exceeded the acceptable values in order to fabricate reliable devices. More samples need to be fabricated, in the same way that was performed in section 4.1, to ensure that the device show similar performances at the same conditions. This work will be continued in the near future by fabricating more samples in order to extract stronger conclusions.

5. Graphene in silicon solar cells

5.1. Graphene as transparent electrode

Graphene is a recent alternative material to be used as transparent electrodes in a variety of applications due to the combination of its unique properties: high transparency, of more than 97.7% for one monolayer of material [199], high carrier mobility, high conductivity and extraordinary mechanical properties, including its ability to bend and stretch. Traditionally, most transparent electrodes are made from transparent conductive oxides, such as indium tin oxide (ITO) and others, and they have several challenges. First of all, its mechanical properties are limiting its applications, as ITO and similar materials are very brittle, and cannot be stretched or bended. Furthermore, there are supply chain issues regarding materials such as indium, a scarce rare earth for which reserves are expected to last only 20 more years.

The rise of new applications, such as bendable and foldable screens, and the explosion in photovoltaic cell technology adoption worldwide must be sufficient motivators to explore other materials. For now, flexible displays are already in the market, while not in large numbers as their price is not competitive yet. These displays currently use as transparent electrode a metallic nanowire mesh, typically made from silver, but also gold, which provides the required conductivity and offers mechanical flexibility.

However, since the discovery of graphene, this material has been called to replace ITO and other materials as a transparent electrode. In the meanwhile, many challenges still need to be solved.

5.1.1. CVD graphene growth and transfer

Large area growth of monolayer graphene continuous films has to be done through chemical vapor deposition. As explained in depth in section 3.1.1, a thin film of pure copper is placed inside the CVD reactor chamber, and given enough temperature and carbon-containing gaseous precursors, such as CH_4, after some minutes the gas molecules crack, in some systems helped by a plasma, and leaves the solid carbon on the surface. Thanks to the high surface temperature of the copper, the carbon can arrange forming crystals of graphene, which after some minutes have covered the entire surface.

In order to separate the graphene film from the copper, chemical etching must be performed. At ISOM a patented automated system is used [174], [175]. After being coated with a thin layer of protective PMMA, the copper/graphene film is placed on an ammonium peroxydisulfate (APS) solution. This chemical slowly etches the copper, and after some time and a thorough cleaning, a graphene/PMMA film is left floating in deionized water. The target substrate to which this graphene layer is to be transferred, can then be placed underneath, submerged in the liquid, and by slowly removing the water, the transfer process is finished. This versatile process can be used to transfer graphene monolayers on any arbitrary surface, with high yield and avoiding manual operation and contamination.

Monolayer graphene has been grown using different CVD recipes. Apart from the continuous monolayer growth, which is ideal for general applications, it is quite difficult to fully characterize the crystalline properties of the graphene film once the growth has been completed. Therefore, for some samples, the growth was stopped earlier, including only the nucleation stage of the graphene grains and allowing them to grow only partially. Together with a post-treatment in hot H_2O_2 to oxidize the graphene/copper films, the samples could be inspected by SEM with high contrast. Hexagonal graphene grains can be seen, and important data such as the nucleation density, the lateral growth speed or the grain size could be extracted by careful image analysis, using a custom program created previously by the group.

As seen in Figure 54, the H_2O_2 treatment helps to distinguish the almost transparent graphene grains from the copper background, as the areas covered by the graphene are protected from oxidation. In Figure 54b, a single crystalline graphene grain with it classic hexagonal shape is shown. The mentioned analysis program first adds more contrast to the image by means of a digital filter, and finally differentiates and classifies those areas (as shown in Figure 54d) in order to perform the required statistics. For the samples used in this work, the average grain size after 5 min of growth was 30 µm in diameter, with a radial growth speed for each grain of around 3 µm per min. The nucleation density was measured to be ~50000 grains/cm^2, assuring the coalescence of the grains after around 8 min of CVD growth. To ensure a complete coverage of the graphene monolayer, the growth for the final graphene samples was maintained for 20 min.

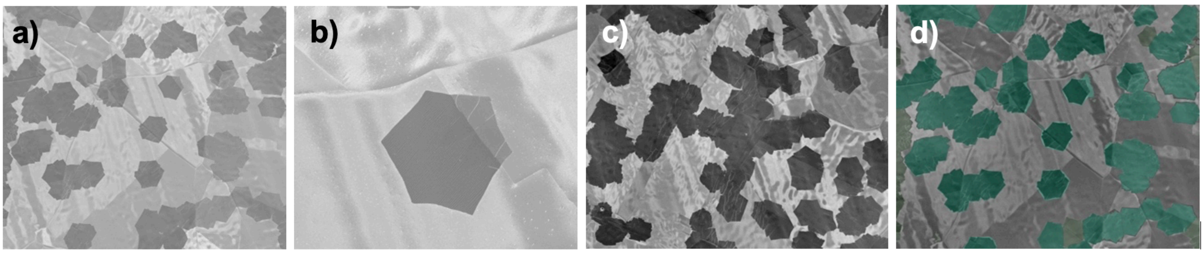

Figure 54: SEM images of the graphene grains after a partial CVD growth and image analysis pipeline. (a) Low magnification. (b) High magnification on a single grain. (c) Pre-processing of the SEM image to increase contrast. (d) SEM image analysis result, from which the growth parameters are extracted.

5.1.2. Graphene field effect transistors

Given that the transparency of the fabricated graphene is given only by its number of layers, the most important parameter left to measure for this intended application is its resistance. For thin films, the concept of sheet resistance emerges, and there are many ways of characterising it. Taking advantage of previous processes developed by the group, the full electrical characterization of the fabricated graphene has been realized using graphene transistors. Graphene transistors, or GFETs, are a special type of transistor in which the channel through which the current passes is a graphene monolayer.

In a regular transistor, the current through the channel is modulated by the presence of a gate, which can be controlled using smaller currents than the ones passing between source and drain. A transistor can act as an amplifier, or just modulate one signal using a different one, and is the base of electronic technology nowadays. Standard semiconductor materials are widely used to fabricate transistors, silicon being the most common choice by far. Thanks to its semiconducting nature, silicon shows a different level of conductivity depending on the available carriers in its crystal structure, and by forcing the inclusion of different elements into the bulk of the material (doping), new carriers can be made available, electrons for n-type, and holes for p-type silicon.

With silicon, a number of transistor architectures have been proposed over the years, and many othersare still being proposed, as the miniaturization scaling of these devices keeps going on, fuelled by the huge demand for faster and more energy efficient electronics. The first one was the bipolar junction transistor, formed by two p-n junctions very close together, which was followed by the current complementary MOS (CMOS) transistor technology, based on metal-oxide-semiconductor (MOS) junctions. These CMOS devices are based on the concept of the field effect transistor or FET, from which graphene transistors were proposed. In a FET, the distribution of charge carriers in the channel are modulated by a gate, which is isolated by an oxide layer, typically SiO_2.

GFETs are based on the same concept, where the graphene monolayer is deposited typically on a SiO_2/Si substrate. In this case, the graphene monolayer acts as the channel, so the source to drain current does not travel through the silicon film. The modulation of the channel is performed through the SiO_2 insulated gate, placed below the graphene layer. This device is capable of a much higher cut-off frequency than standard silicon FETs, and the two-dimensional nature of graphene made it ideal to fabricate sensing devices. However, the structure is also ideal to characterise electrically the graphene, as the modulation of its conductivity by a gate voltage allows to extract magnitudes such as the position of the Fermi level of the graphene and the unintentional doping it achieved during processing, as well as its conductivity, sheet resistance and other basic parameters.

It's fabrication process is also rather simple and is schematically shown in Figure 55. One metallization and lift-off step is enough to define metallic contacts on a Si/SiO_2 wafer, and graphene can be conformally transferred on top. An extra lithography step is required to define the graphene channels, which are isolated using inductive coupled plasma etching using oxygen. After removing the ICP resist protecting layer, in order to homogenize the properties of the graphene layer, an annealing step is required. The annealing is performed at 280ºC in a tubular oven, in the presence of a nidron (non-flammable mix of hydrogen in nitrogen) flow, at ambient pressure. Through this step, the possible residues attached to the graphene are reduced, and the transferred monolayer gets more conformally attached to the substrate below.

The small dimensions of such devices allow to fabricate many of them on a single die, which is useful to perform statistical data analysis on the measurements, to smooth the high variability intrinsic to 2D materials. Furthermore, the exposed graphene layer on top of the transistor structure allows to continuously characterize the device as the following process steps are performed, such as chemical doping of the graphene layer or device encapsulation.

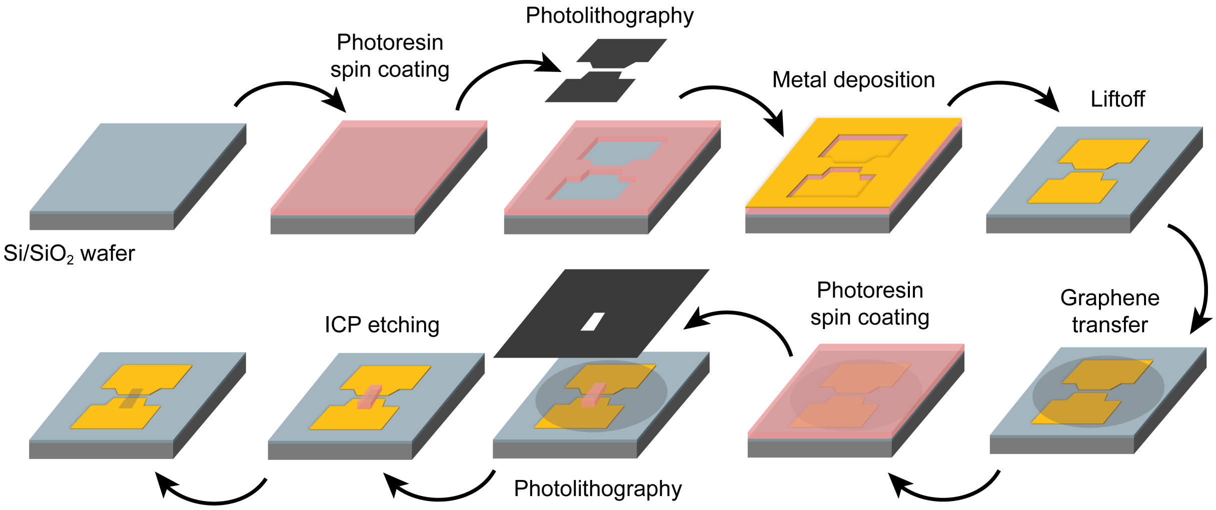

Figure 55: Schematic drawing of GFET transistor microfabrication process.

GFET characterization is performed through standard 3 terminal measurements using a probe station and a semiconductor analyzer (Figure 56a), which monitors the source-drain current with a variable gate voltage. During the measurement the gate current is monitored to avoid short-circuits indicative of device breakage. The IV data, taken from a set of GFET devices with different channel lengths, allows to extract the required parameters, which are analyzed using a custom python program previously developed in the group.

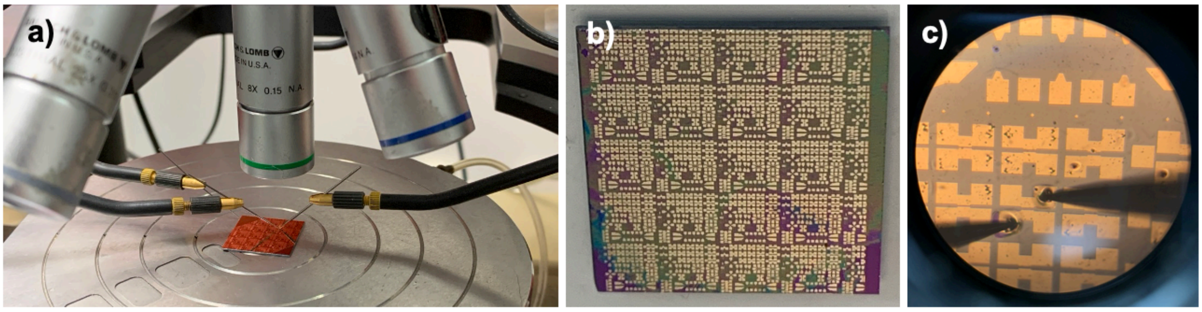

Figure 56: GFET transistors and measurement set-up. (a) Probe station measurement setup, using three terminals. (b) Final silicon die with many GFET devices (c) Close-up of the GFET being measured, through the optical microscope.

To characterize the deposited graphene layer, a photolithography mask was designed. This mask contains a matrix of patterns, each with 16 GFETs of different dimensions, with channel length ranging from 10 to 50 µm. In a 20x20 mm silicon die, over 20 regions can be fitted, including over 100 transistors, as seen in Figure 56b. This high density of devices was designed to be very flexible, allowing to distinguish, for example, spatial variabilities such as the electrical properties of the edge and the center of the transferred graphene monolayer, which can have different growth parameters. For the characterization performed in this experiment, between 30 and 60 GFETs for each silicon die were measured, as seen in Figure 57, more than enough to characterize the electronic quality of the graphene monolayer.

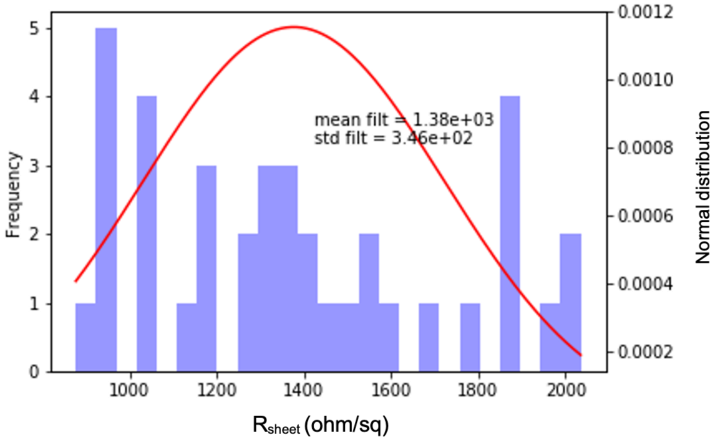

Figure 57: Histogram of electrical measurements for sample S275-3. (30 GFETs), no extra processing steps. In blue columns, the frequency of R_{sheet} measurements; in red, the normal distribution.

5.1.3. Graphene doping with $AuCl_3$

As mentioned in section 2.4.4, chemical doping is one of the key strategies to improve the electrical properties of graphene. Graphene presents an extremely high carrier mobility, due to its unique electronic band structure and crystal quality. However, the density of carriers at the Fermi level gets close to zero, making it highly resistive at that non-biased level. Therefore, the macroscopic properties of graphene regarding its conductivity have limited its application in many fields.

Graphene's sheet resistance is governed by two parameters, the carrier mobility (μ) and the carrier concentration (n) by the following expression, where μ is expressed in cm^2/Vs, and n in cm^{-2}:

$$R_{sheet} = \frac{1}{q \cdot \mu \cdot n} \tag{5.1}$$

In previous sections, the many possible dopants of graphene have been mentioned, from chemicals in vapor form, to metallic nanoparticles. Here in this study, $AuCl_3$ nanoparticles have been used. The use of gold chloride nanoparticle as a dopant for graphene was proposed by Kim et al. [200], who achieved a 77% reduction in sheet resistance, up to 150 Ω/sq for monolayer graphene, by spin coating $AuCl_3$ dissolved in nitromethane, a very volatile solvent. The objective of this work was to deepen the knowledge of the group in graphene technology, adapting a proven method for graphene doping and study its degradation over time. Adding to this, the ultimate goal was to propose strategies to lock the doping particles on the graphene and avoid, or at least delay, its degradation.

For the characterization of the graphene doping and its degradation, the electrical characteristics of several doped graphene transistors were measured with time to observe any changes. The measurements were made in 30 devices, every few h at the beginning, and every few days later. The different measurements of the unprotected doped transistors are shown in Figure 58.

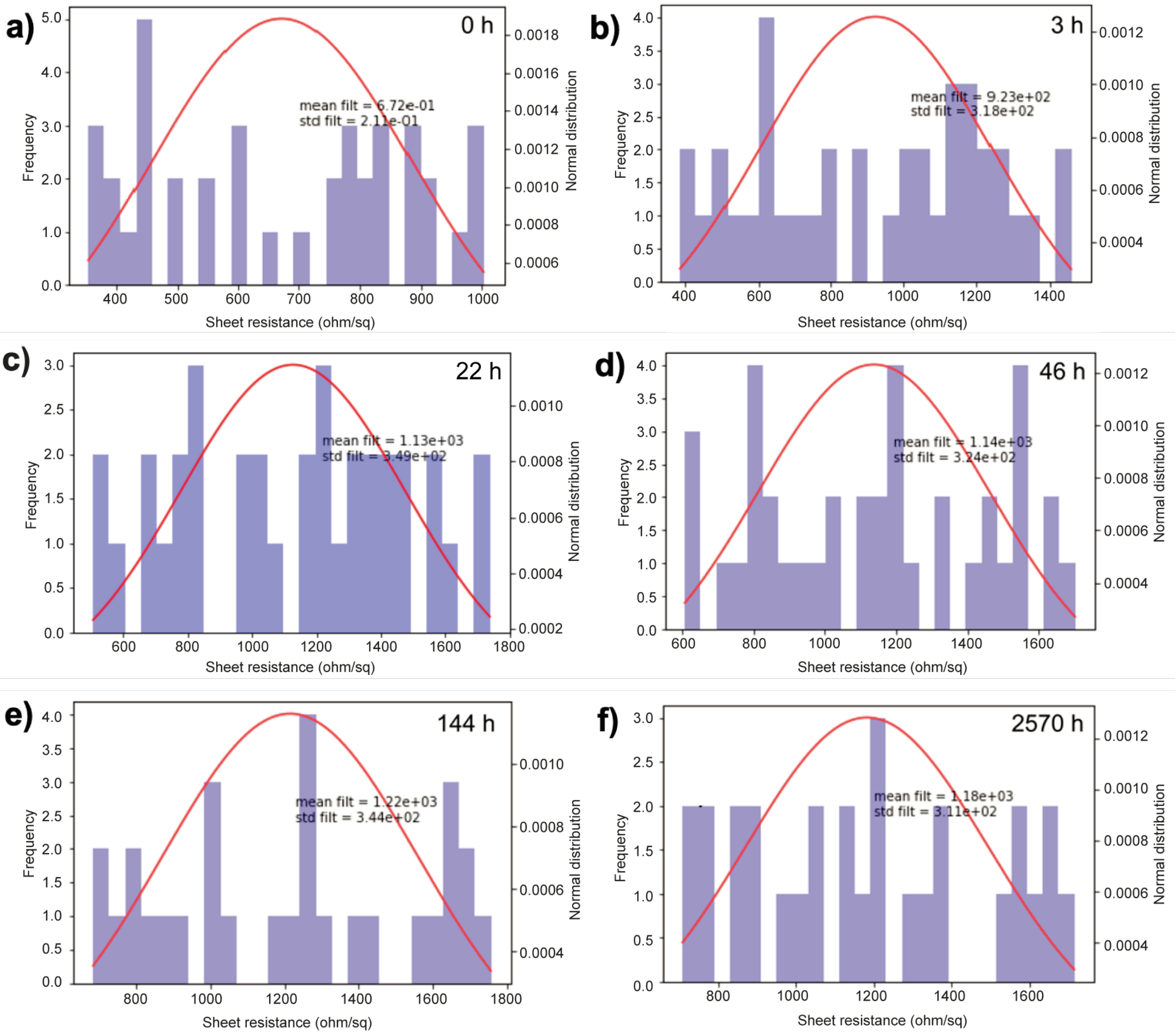

Figure 58: Sheet resistance histograms for sample "A" (S275-3) doped and unprotected. (a-f) Histograms showing the sheet resistance evolution with time of the graphene transistors, from 0 h to 2570 h.

Sample S275-3 (A), doped and left unprotected, shows a great improvement right after doping, with the sheet resistance going down from the original 1380 ohm/sq (Figure 57) to 672 Ω/sq immediately after. It took less than one day to bring the sheet resistance over 1000 ohm/sq, and after 22 h, the measured value was 1130 Ω/sq. After 6 days, or 144 hours, 1220 Ω/sq, the value was still slightly below the undoped one, and it kept the small improvement for 100 more days, the last measurement being 1180 Ω/sq after 2570 h.

5.1.4. Doping encapsulation with PDMS thin films

It is clear that doping graphene with Au nanoparticles is beneficial for the sheet resistance, although the improvement fades quickly with time. However, it is necessary to protect the doped device a with layer which could trap those particles and isolate them from the degrading agents in the atmosphere, which for most dopants is humidity.

The proposed encapsulation technique to protect the doping without degrading its optical and electrical properties was the coverage with polydimethylsiloxane (PDMS), a silicone-based transparent polymer. Using PDMS, two strategies were tested. First, the direct spin-coating of the doped graphene transistors, baking and setting the PDMS on the chip. As this strategy was expected to interfere to some extent with the applied doping, a second strategy was developed, consisting on the fabrication of free-standing PDMS thin films using a lift-off method, as described in Figure 59. The dry PDMS thin film was then placed on top of the doped graphene transistors, and conformally attached to the substrate using light vacuum.

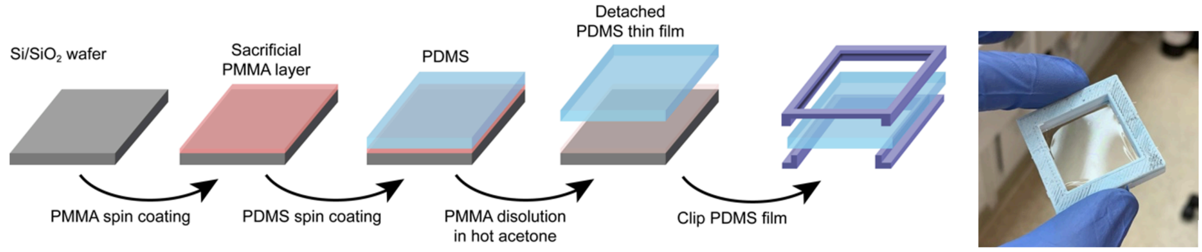

Figure 59: Schematic drawing of the PDMS thin film fabrication process, and picture of the final fabricated PDMS thin film.

All three samples, the unprotected (sample A), the protected with spin-coated PDMS (sample B) and the protected with thin-film PDMS (sample C) were fabricated and measured over a span of 100 days, the last measurement being taken around 2500 h after the doping. The same measurements as the ones shown in Figure 58 were performed for samples B and C, and the sheet resistance results are plotted in Figure 60 for clarity. Figure 60a shows the raw average values of the sheet resistance, and Figure 60b shows the same values normalized by the initial undoped R_{sheet} value for each sample. In both cases, lower is better.

Sample A and B are both part of the same graphene transfer piece, labelled S275-3, while sample C used graphene S275-4, part of the same S275 growth, but transferred as a different piece, at a different time. The as-transferred R_{sheet} value, post-annealing, for samples A and B is 1380 Ω/sq, while for sample C, the value was much higher at 2030 Ω/sq. After this measurement, samples were doped using the same 10 mmol $AuCl_3$ solution and protected accordingly.

The blue diamond symbols represent sample A, with a marked reduction in R_{sheet} right after the doping, of around 50% of the original value. However, the doping particles get degraded over time and after 20 h, the resistance value increases up to around 85% for the rest of the experiment. For the protected samples, the trends are slightly different. Sample B did not show any relevant reduction in the sheet resistance, with values of around 90% of the original one. This can hint to a removal of the doping particles by the same protecting layer, as the PDMS layer was spin-coated in its liquid form, partly removing the Au nanoparticles in the process, or reducing its effect.

However, sample C, protected with a dry PDMS thin film, shows much better results. 4 h after doping, the sheet resistance was still of 900 Ω/sq, 44% of the original value. Furthermore, this low resistance level is kept for the first hours, as at 25 h, the measured value was the minimum of the series at 841 Ω/sq or 41%. For the next measurements, the values increase slightly, but to percentages of around 50%, much better than the other two samples. The last measurement, after 2500 h, shows an increase of the sheet resistance up to 1440 Ω/sq or 71%, still considerably better than samples A and B.

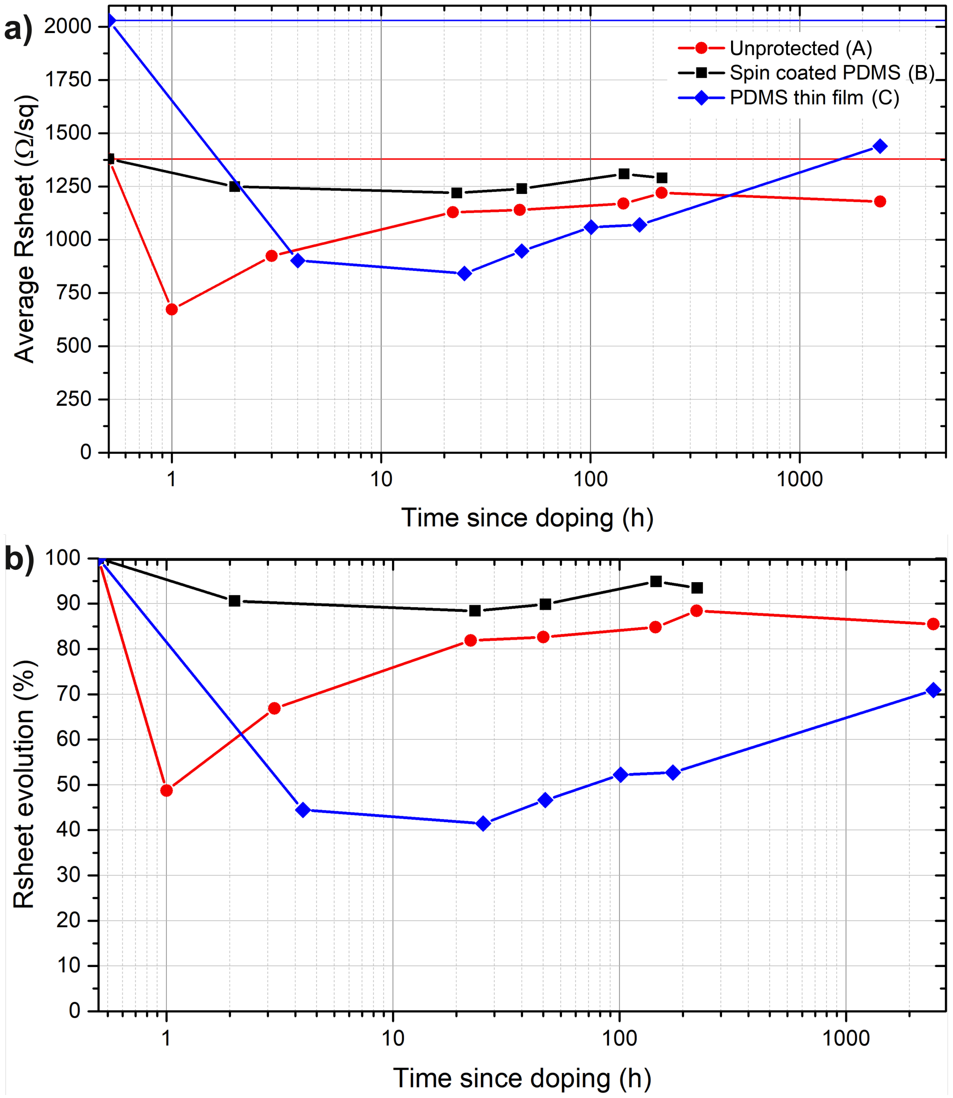

Figure 60: Graphene sheet resistance evolution with time, for three doped samples, all with 10 mmol $AuCl_3$ spin coated. Sample A (red, circles) was exposed to air, not protected. Sample B (black, squares) was protected with spin coated PDMS. Sample C (blue, diamonds) was protected with a transfered PDMS thin film. (a) Absolute R_{sheet} values, averaged. Colored horizontal lines mark the initial R_{sheet} values for A, B and C samples. (b) R_{sheet} values expressed normalized by the initial value for each sample before doping.

A last comment must be made, as these experiments were heavily affected by the lockdown caused by the COVID-19 pandemic. The large gap between the two last measurements, at around 150 h and 2500 h is explained by the inability of accessing the labs between these times. After the access to the labs was re-established, the samples were measured one last time. However, the limited access to the equipment and time restrictions, made it difficult to continue with the series of measurements or to fabricate new samples, leaving the experiment without strong conclusions. However, these results, as well as the PDMS thin film strategy, which is very promising once fully optimized, will serve as base work for a future PhD research focused on graphene for transparent electrodes and solar cells, which is currently underway.

5.2. First Schottky solar cells

In order to explore new applications of graphene, a small line of work was set up to fabricate graphene/silicon Schottky solar cells using the expertise that the group had in both microfabrication and graphene technology. These devices would serve as a benchmark to test the effect of the different graphene processing steps in the performance of solar cell devices, and are integrated within the DIGRAFEN and REGRAP-2D projects. This study has been realized thanks to a close collaboration with CIEMAT, jointly processing and characterizing the devices.

Schottky solar cells (SSC) have been introduced in section 2.4.4. To quickly introduce these devices, they consist of a graphene layer deposited on top of a silicon window, forming a diode, a Schottky junction. A top contact shaped as a ring access the graphene layer, and a back contact is placed on the back side of the silicon wafer. Many elements affect the performance of these devices, the most critical ones being the quality and electrical properties of the graphene layer, and the interface between graphene and silicon.

The general fabrication process for graphene/silicon SSCs is outlined in Figure 61, starting with a Si/SiO_2 wafer. First, the back contact is deposited, and the rest of the processing steps will keep to the front side. The front contact is then deposited through photolithography and lift-off, and a second lithography step defines the area for the silicon window. The window was opened using buffered hydrofluoric acid (BHF), a mixture of HF and NH_4F in 1:10 ratio, to etch the SiO_2 layer. After that, the graphene layer is transferred on top of the window and metallic ring, immersing the sample in DIW as part of the transfer process. The time between the etching and the graphene transfer step was monitored, to fix the amount of native SiO_2 that grows on the etched window. The process leaves a very thin layer of SiO_2 on top of the opened silicon window. It is unavoidably grown natively by oxygen and water exposure, between the BHF etching and the graphene transfer. Once the graphene has been transferred, the graphene is patterned by photolithography and ICP etching. However, for the devices presented in this work, this step could not be completed due to equipment limitations, so the devices were isolated manually using a diamond tip.

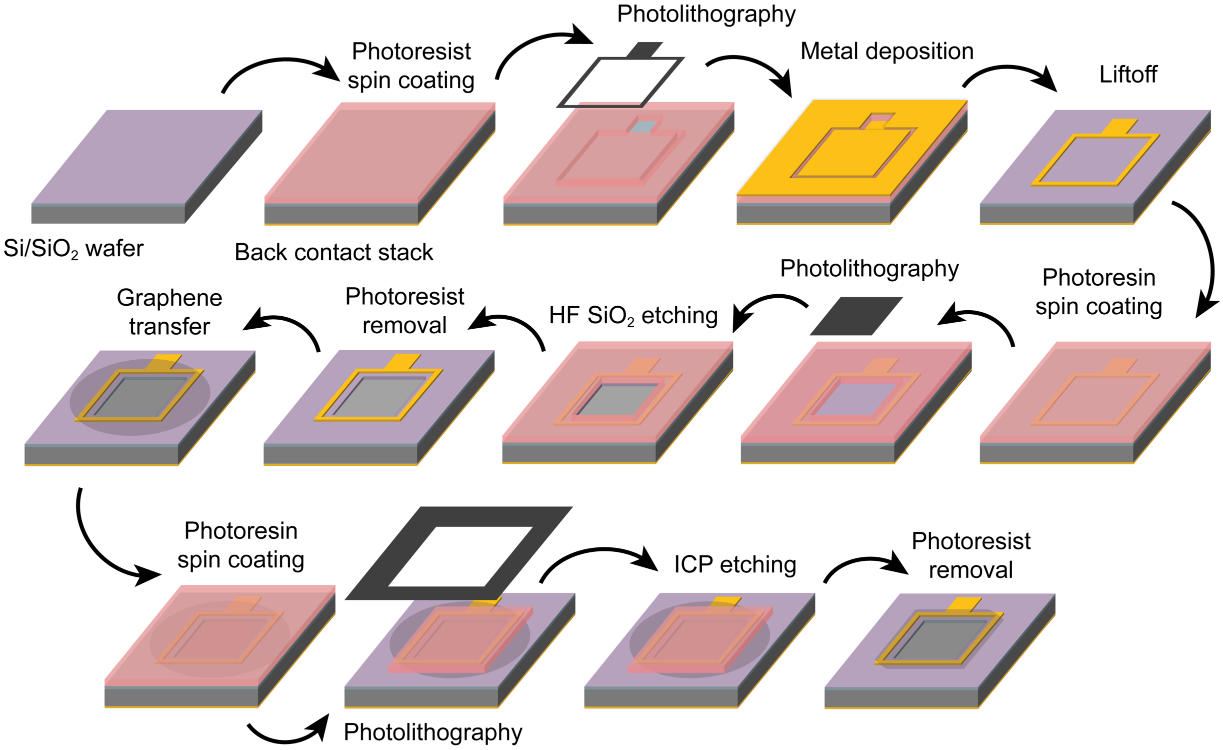

Figure 61: Schematic drawing of the main processing steps for the fabrication of a graphene/silicon Schottky solar cell.

To gain some insight on the process' most critical steps, some initial studies were made on silicon oxide etching using BHF. The etching process is rather simple, immersing the wafer in the solution, moving slowly the sample to increase the access fresh BHF is enough. After some minutes, a clear change in the hydrophobicity of the opened window marks the completion of the etching process. This step was characterized using several dummy samples etched for different durations and measuring the step size with a profilometer. The SiO_2 thickness of the used wafers was 300 nm, and after 7 min, the silicon underneath was reached, as seen in Figure 62.

The etch rate was measured to be linear, around 43.5 nm/min, and once it was known, the first prototypes were produced. The first prototype, SSC1, failed, not producing the required diode in dark. For this device, the selected back contact was a Cr/Au stack, and the silicon wafer used had a rough, not polished back side, which was not standard for solar cell manufacturing. A second device, SSC2 was fabricated using the same back contact and silicon wafer, and its I-V characteristics under illumination were measured successfully and plotted in purple in Figure 63. With a J_{SC} of 84 μA/cm², a V_{OC} of 0.285 and a fill factor of 0.15, the efficiency is almost negligible, pointing at wrong material choices or mistakes during processing.

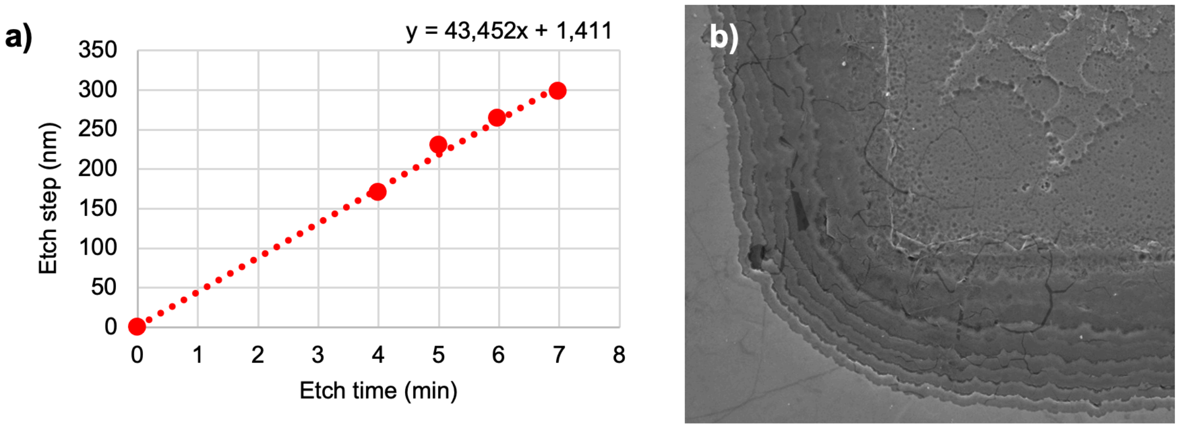

Figure 62: (a) Thickness of the SiO_2 etched step with time. (b) SEM image of the etched edge of SSC2.

In order to achieve better performances, the back contact was modified. With the help of CIEMAT photovoltaics unit, a standard back-contact stack for silicon wafers was used, consisting of a thin layer of intrinsic amorphous silicon (a-Si), followed by a layer of n-type a-Si and finished with two metal layers of titanium to promote adhesion and gold for good electrical connexion. The rough n-type silicon wafer was kept, so the modification of the back-contact alone, improved greatly the behaviour of SSC3 as can be seen in Figure 63. In yellow (dotted line), the I-V curves under illumination of the as-fabricated SSC3 is shown, with an efficiency of 0.26% thanks to the improved J_{SC} up to 0.7 mA/cm^2, although the V_{OC} is slightly reduced. The yellow line corresponds to the same sample, once it has been doped and protected with a thin PDMS film as explained in the previous section. Both J_{SC} and V_{OC} are clearly improved by the doping, reaching an efficiency of 0.475%.

However, the shape of the I-V curve is far from what is expected for a solar cell. This feature, which can be described as an S-shaped curve, has been previously described for many types of solar cells, where a mismatch between the absorber layer and the charge extraction layers is found. This means that the back contact stack needs to be further optimized, but the main issue lays in the graphene layer characteristics and doping level. Following these strategies, the S-shape can be fully mitigated [201]. Specifically, for Schottky solar cells, the shape can be corrected by a combination of annealing and doping [202].

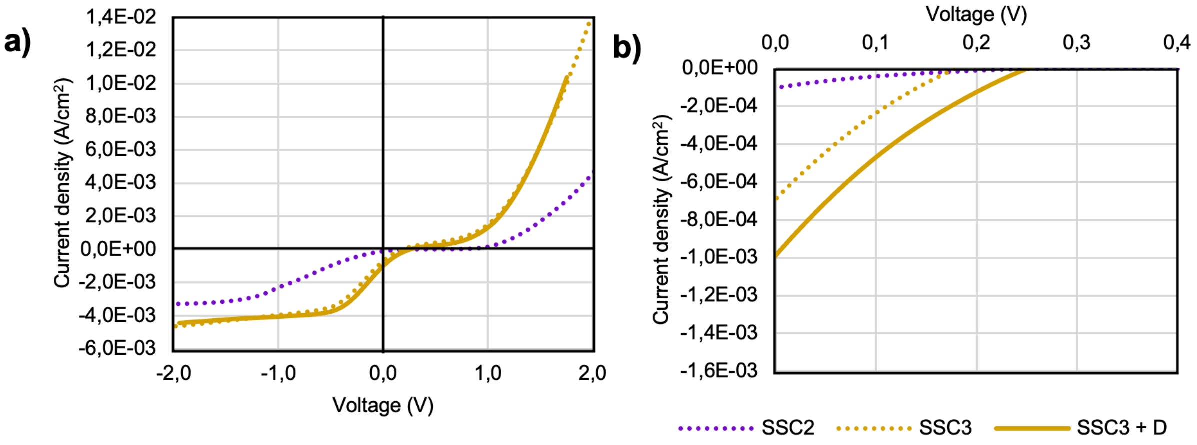

Figure 63: I-V characterization under 1.5AM illumination of samples SSC2, SSC3 and SSC3 after doping. (a) I-V curve from -2 to 2 V. (b) Zoomed region from 0 to 0.4 V.

In Figure 64, the dark I-V characteristics of SSC4 are shown. SSC4 is a similar device as SSC3, using the same back contact stack and similar graphene, but applying an annealing step before the doping. Figure 64 shows in dashes the as-fabricated dark characteristics of the solar cell, and in dots the same device after being annealed for 2 min at 400ºC in forming gas. The improvement of the dashed line is clear, with a much flatter shape at negative voltages, showing a promising diode behaviour before doping.

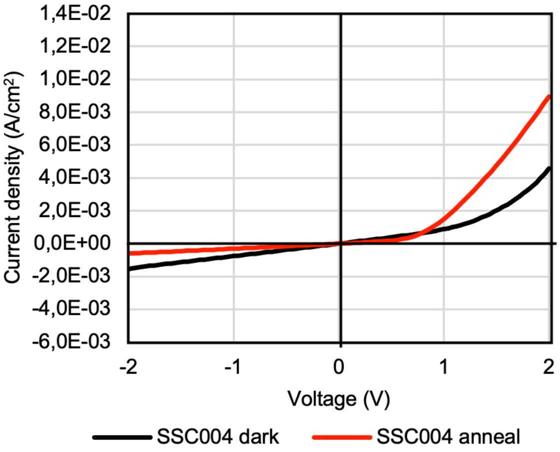

Figure 64: I-V characterization in dark of sample SSC4, before and after annealing.

SSC4 was then doped using the same $AuCl_3$ recipe, and protected using a PDMS thin film. The I-V characteristics of all the stages of SSC4 are shown in Figure 65. The improvement achieved by the doping is noticeable, even more as the first measurement of SSC4 before annealing or doping barely produced any current. Once the sample as annealed, the characteristics improved to 0.77 mA/cm² and 0.29 V of J_{SC}

and V_{OC} respectively, with a fill factor of 0.178 and an efficiency of 0.4%, similar to the value the doped SSC3 sample achieved. By doping, the characteristics improved even more, pushing both J_{SC} and V_{OC} to 1.39 mA/cm² and 0.378 V. This sample, while keeping the same fill factor of 0.178, reached an efficiency of 0.94%.

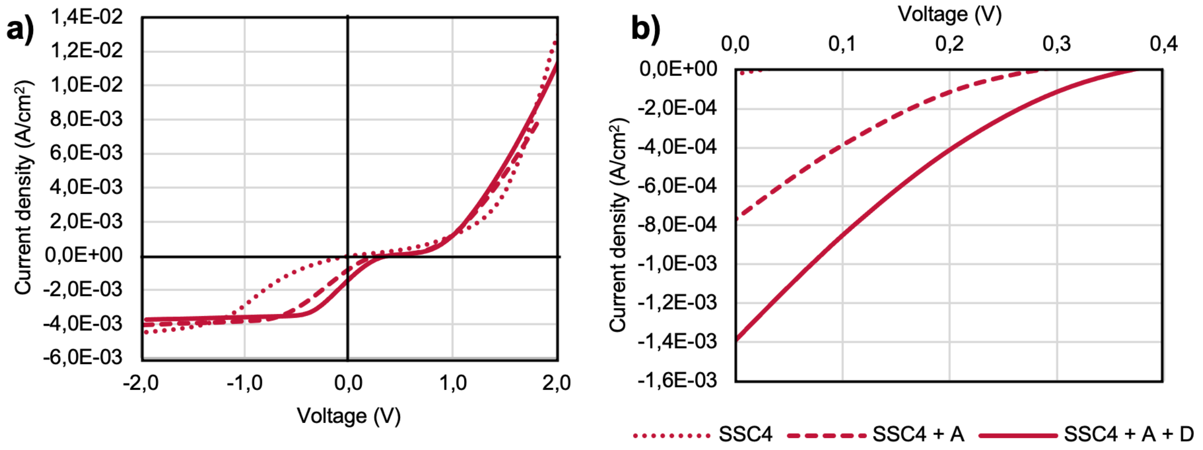

Figure 65: I-V characterization under AM1.5G illumination of samples SSC4, SSC4 after annealing and SSC 4 after annealing and doping. (a) I-V curve from -2 to 2 V. (b) Zoomed region from 0 to 0.4 V.

To finish the comparison, SCC3 and SSC4, both fabricated using the same materials and process, and both after doping, have been plotted in Figure 66. The difference between them is that SSC4 was annealed before doping. While the annealing step did not change abruptly the shape of the curve, it can be considered as a step in the right direction.

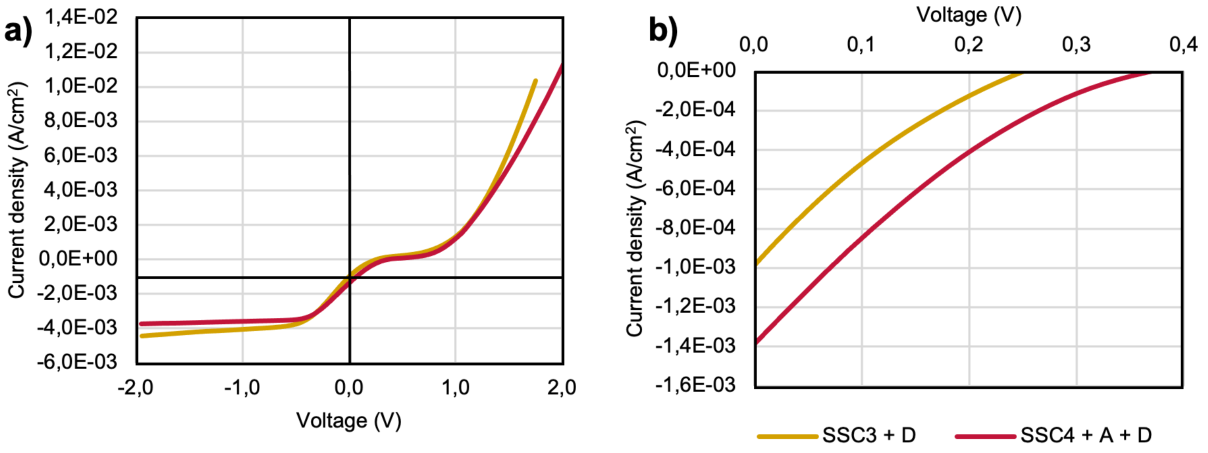

Figure 66: I-V characterization under AM1.5G illumination of samples SSC3 after doping and SSC4 after annealing and doping.I-V curve from -2 to 2 V. (b) Zoomed region from 0 to 0.4 V

ID	J_{SC} (mA/cm²)	V_{OC} (V)	FF	η	R_{sheet} (Ω/sq)	Info
SSC1	-	-	-	-	-	No diode
SSC2	0,08442	0,285	0.15	0.037%	-	BC: Cr/Au
SSC3	0,6994	0,182	0.206	0.26%	-	BC: a-Si (i) / a-Si (n) + Ti/Au
SSC3 + doping	0,9979	0,257	0.185	0.475%	-	BC: a-Si (i) / a-Si (n) + Ti/Au D: $AuCl_3$ 10mM NPs
SSC4	0,023	0,024	~ 0	~ 0 %	1360	BC: a-Si (i) / a-Si (n) + Ti/Au
SSC4 + annealing	0,77	0,29	0,178	0.40%	1250	BC: a-Si (i) / a-Si (n) + Ti/Au A: 400ºC, 10 min in nidron
SSC4 + annealing + doping	1,39475	0,378	0,178	0,94%	977	BC: a-Si (i) / a-Si (n) + Ti/Au A: 400ºC, 10 min in nidron D: $AuCl_3$ 10mM NPs

Table 3: Summary of electrical properties of the fabricated Schottky Solar Cells. BC: back contact; D: doping; A: annealing.

6. Conclusions and future work

In this thesis, two main areas of work have been considered. On one hand, the use of graphenic materials for energy storage in supercapacitors, specifically through the fabrication of laser induced graphene microsupercapacitors, complemented with pseudocapacitive elements. And on the other hand, the use of monolayer graphene in solar cells, studying its potential as a transparent electrode and integrated in graphene/silicon Schottky solar cells. For the first project, the results were successfully published in scientific journals, and for the latter one, the exploratory nature of the projects yielded promising results which served as a base for future projects within the group.

Regarding the energy storage area, the results have been published in several research papers. These include the evaluation of the main trends in the supercapacitor research field, identifying laser writing as a very promising technique to fabricate microsupercapacitors. In that study it was also shown that complementing those supercapacitors with metallic and bimetallic oxides and sulfides was the best approach to increase its energy density without compromising its power. Furthermore, the development of microsupercapacitors opens new applications as power sources on flexible and wearable electronics.

From there, laser writing technique was applied in the lab to fabricate laser induced graphene, which was optimized for its use in microsupercapacitors. Laser writing is proposed as a fast, flexible and accessible technique to fabricate high-quality, thin-film, 3D graphene networks. In that study, interdigitated microsupercapacitors with a capacitance of over 22 mF/cm^2 were fabricated, through thorough study of the material quality and microstructure of the LIG used. The performance of the fabricated devices, in capacitance, but also in energy and power density, is among the highest for a pure-carbon, EDLC supercapacitor made from LIG. Furthermore, higher voltage configurations using the optimized LIG material were produced, measured, and finally integrated with the electronics developed at CIEMAT.

Finally, during an international research stay, the addition of pseudocapacitive nanoparticles to the microsupercapacitors was tested, using MoS_2 nanoflakes to produce nanosized molybdenum oxides through laser irradiation. MoO_2 nanoparticles were produced on top of the LIG microsupercapacitors, which were measured using an ionic liquid electrolyte in an oxygen and humidity free atmosphere. This addition increased the capacitance up to 35 mF/cm^2 at 0,04 mA/cm^2 and the energy density up to 25 µWh/cm^2 at the same current. These values are better than what could be expected theoretically by measuring the best bare LIG microsupercapacitor in ionic liquid. The study yielded promising results, which will guide future experiments.

Regarding the second area of this thesis, a first topic was dedicated to advancing general graphene technology. Chemical doping of graphene and its protection for better durability was studied, using $AuCl_3$ nanoparticles, which was confirmed to effectively dope the graphene, reaching improvements of the sheet resistance of more than 60%. An approach for protecting the doping using thin films of PDMS was tested, which partially kept the doping activity for more than 100 days. That technology was later applied to the fabrication of Schottky solar cells, which after several prototypes and the optimization of the most critical processing steps, an efficiency of 1% was reached. While the efficiency can still be improved, mostly through the optimization of the graphene quality and the doping, the establishment and validation of the processing steps serves as a starting point for future iterations.

6.1. Future prospects for graphene in energy storage

One of the main topics worth to keep investigating after this thesis is the continued optimization of LIG material fabricated on flexible substrates. The LIG shown in this work as all fabricated on flexible polyimide films, which are strongly attached to solid glass support plates. This allowed for easy manipulation and less sample-to-sample variability; however it eliminated one of the main advantages of LIG, its flexibility. The mechanical properties of the substrate material and its effect on the electrochemical properties of the microsupercapacitors, including the effect of the electrolyte as structural support, are already being investigated. Two master thesis have been devoted to this topic at the ISOM-UPM laboratory, testing different methods to transfer the LIG material to other substrates such as PDMS, which are not only flexible, but also stretchable. With this, devices such as strain or bending sensors have been developed.

Another interesting topic is the fabrication of more compact micosupercapacitor stacks for higher voltage applications. Exploiting the use of thin polyimide substrates and avoiding the use of thicker support structures, high voltage stacks can be made in a much more compact way, allowing to increase the current rating of the fabricated devices. It is also possible to explore the use of larger polyimide substrates to connect in parallel the devices in an integrated way using LIG as well.

As a continuation of the work in complementing the LIG material with pseudocapacitive elements, a priority would be to finish the MoS_2 experiment to obtain stronger conclusions, fabricating more samples to account for sample variability and molybdenum mass loading. Understanding the role of the size and shape of the precursor MoS_2 nanoparticles in the transformed molybdenum oxides and their redox pseudocapacitance is an interesting topic. In the same area, other nanostructured pseudocapacitive materials can also be proposed to complement graphene supercapacitors.

Finally, a topic which was proposed before, is to explore the potential of LIG to fabricate other devices such as heaters or sensors, which could be integrated in the same polymer substrate for flexible and wearable electronics.

6.2. Future prospects for graphene for solar cells

In the area of solar cells and transparent electrodes based on graphene, a first topic would be the exploration of different dopants for improving the electrical properties of graphene and its applications as a transparent electrode. These dopants should be effective, have good stability in ambient conditions and not interfere with graphene’s optical properties. Silver nanowires are one of the most promising ones, bridging the graphene grains and adding a flexible network improving conductivity and doping the graphene. This experiment has already started at the group.

If still the dopants need to be protected, the development of a protection strategy using multi-layered polymeric films is expected to improve the actual level of protection. This way, the thin films would block even better the oxygen and humidity, using as a base the PDMS thin film process presented in this thesis. On top of that, a different strategy would be to nanostructure the encapsulating PDMS film, using nanoimprint lithography or other techniques. This way the protecting layers would become multifunctional, acting as an antireflective coating too and improving the solar cell characteristics.

Within the topic of Schottky solar cells, the use of other 2D materials such as MoS_2 as an interlayer between the graphene and the silicon is to be explored, benefiting the charge separation and avoiding recombination by passivating the interface. Furthermore, a modification of the automatic graphene transfer process can be proposed so it works faster at depositing two graphene layers. On a different approach, as the transfer process now is based on the immersion of the target substrate, dopants that can survive the process are needed. If this cannot be established, a dry transfer process of the graphene layers can be proposed.

References

[1] K. S. Novoselov *et al.*, “Electric Field Effect in Atomically Thin Carbon Films,” *Science (1979)*, vol. 306, no. 5696, pp. 666–669, Oct. 2004, doi: 10.1126/science.1102896.

[2] “Goal 11 | Department of Economic and Social Affairs.” Accessed: Sep. 19, 2023. [Online]. Available: https://sdgs.un.org/goals/goal11

[3] E. Estrada, M. P. Martínez Vargas, J. Gómez, A. Peña Pérez Negron, G. L. López, and R. Maciel, “Smart Cities Big Data Algorithms for Sensors Location,” *Applied Sciences*, vol. 9, no. 19, p. 4196, Oct. 2019, doi: 10.3390/app9194196.

[4] R. Hidalgo-Leon *et al.*, “Powering nodes of wireless sensor networks with energy harvesters for intelligent buildings: A review,” *Energy Reports*, vol. 8. Elsevier Ltd, pp. 3809–3826, Nov. 01, 2022. doi: 10.1016/j.egyr.2022.02.280.

[5] J. Kang, W. Cao, X. Xie, D. Sarkar, W. Liu, and K. Banerjee, “Graphene and beyond-graphene 2D crystals for next-generation green electronics,” T. George, M. S. Islam, and A. K. Dutta, Eds., Jun. 2014, p. 908305. doi: 10.1117/12.2051198.

[6] H. W. Kroto, J. R. Heath, S. C. O’Brien, R. F. Curl, and R. E. Smalley, “C60: Buckminsterfullerene,” *Nature*, vol. 318, no. 6042, pp. 162–163, Nov. 1985, doi: 10.1038/318162a0.

[7] G. Yu, J. Gao, J. C. Hummelen, F. Wudl, and A. J. Heeger, “Polymer Photovoltaic Cells: Enhanced Efficiencies via a Network of Internal Donor-Acceptor Heterojunctions,” *Science (1979)*, vol. 270, no. 5243, pp. 1789–1791, Dec. 1995, doi: 10.1126/science.270.5243.1789.

[8] C.-Z. Li, H.-L. Yip, and A. K.-Y. Jen, “Functional fullerenes for organic photovoltaics,” *J Mater Chem*, vol. 22, no. 10, p. 4161, 2012, doi: 10.1039/c2jm15126j.

[9] A. W. Jensen, S. R. Wilson, and D. I. Schuster, “Biological applications of fullerenes,” *Bioorg Med Chem*, vol. 4, no. 6, pp. 767–779, Jun. 1996, doi: 10.1016/0968-0896(96)00081-8.

[10] S. Iijima, “Helical microtubules of graphitic carbon,” *Nature*, vol. 354, no. 6348, pp. 56–58, Nov. 1991, doi: 10.1038/354056a0.

[11] M. Monthioux and V. L. Kuznetsov, "Who should be given the credit for the discovery of carbon nanotubes?," *Carbon N Y*, vol. 44, no. 9, pp. 1621–1623, Aug. 2006, doi: 10.1016/J.CARBON.2006.03.019.

[12] L. V. Radushkevich and V. M. Lukyanovich, "The Structure of Carbon Forming in Thermal Decomposition of Carbon Monoxide on an Iron Catalyst," *Russian Journal of Physical Chemistry*, vol. 26, no. 1, pp. 88–95, 1952.

[13] T. W. Odom, J.-L. Huang, P. Kim, and C. M. Lieber, "Structure and Electronic Properties of Carbon Nanotubes," *J Phys Chem B*, vol. 104, no. 13, pp. 2794–2809, Apr. 2000, doi: 10.1021/jp993592k.

[14] M. Fujita, K. Wakabayashi, K. Nakada, and K. Kusakabe, "Peculiar Localized State at Zigzag Graphite Edge," *J Physical Soc Japan*, vol. 65, no. 7, pp. 1920–1923, Jul. 1996, doi: 10.1143/JPSJ.65.1920.

[15] K. Nakada, M. Fujita, G. Dresselhaus, and M. S. Dresselhaus, "Edge state in graphene ribbons: Nanometer size effect and edge shape dependence," *Phys Rev B*, vol. 54, no. 24, pp. 17954–17961, Dec. 1996, doi: 10.1103/PhysRevB.54.17954.

[16] K. Wakabayashi, M. Fujita, H. Ajiki, and M. Sigrist, "Electronic and magnetic properties of nanographite ribbons," *Phys Rev B*, vol. 59, no. 12, pp. 8271–8282, Mar. 1999, doi: 10.1103/PhysRevB.59.8271.

[17] D. V. Kosynkin *et al.*, "Longitudinal unzipping of carbon nanotubes to form graphene nanoribbons," *Nature*, vol. 458, no. 7240, pp. 872–876, Apr. 2009, doi: 10.1038/nature07872.

[18] L. Jiao, L. Zhang, X. Wang, G. Diankov, and H. Dai, "Narrow graphene nanoribbons from carbon nanotubes," *Nature*, vol. 458, no. 7240, pp. 877–880, Apr. 2009, doi: 10.1038/nature07919.

[19] L. Jiao, X. Wang, G. Diankov, H. Wang, and H. Dai, "Facile synthesis of high-quality graphene nanoribbons," *Nat Nanotechnol*, vol. 5, no. 5, pp. 321–325, May 2010, doi: 10.1038/nnano.2010.54.

[20] J. Cai *et al.*, "Atomically precise bottom-up fabrication of graphene nanoribbons," *Nature*, vol. 466, no. 7305, pp. 470–473, Jul. 2010, doi: 10.1038/nature09211.

[21] C. Lee, X. Wei, J. W. Kysar, and J. Hone, "Measurement of the Elastic Properties and Intrinsic Strength of Monolayer Graphene," *Science (1979)*, vol. 321, no. 5887, pp. 385–388, Jul. 2008, doi: 10.1126/science.1157996.

[22] K. S. Novoselov *et al.*, “Two-dimensional gas of massless Dirac fermions in graphene,” *Nature*, vol. 438, no. 7065, pp. 197–200, Nov. 2005, doi: 10.1038/nature04233.

[23] S. V. Morozov *et al.*, “Giant Intrinsic Carrier Mobilities in Graphene and Its Bilayer,” *Phys Rev Lett*, vol. 100, no. 1, p. 016602, Jan. 2008, doi: 10.1103/PhysRevLett.100.016602.

[24] J.-H. Chen, C. Jang, S. Xiao, M. Ishigami, and M. S. Fuhrer, “Intrinsic and extrinsic performance limits of graphene devices on SiO2,” *Nat Nanotechnol*, vol. 3, no. 4, pp. 206–209, Apr. 2008, doi: 10.1038/nnano.2008.58.

[25] G. Bottari *et al.*, “Chemical functionalization and characterization of graphene-based materials,” *Chem Soc Rev*, vol. 46, no. 15, pp. 4464–4500, 2017, doi: 10.1039/C7CS00229G.

[26] J. M. Fernández-García, P. Izquierdo-García, M. Buendía, S. Filippone, and N. Martín, “Synthetic chiral molecular nanographenes: the key figure of the racemization barrier,” *Chemical Communications*, vol. 58, no. 16, pp. 2634–2645, 2022, doi: 10.1039/D1CC06561K.

[27] R. Otero, J. M. Gallego, A. L. V. de Parga, N. Martín, and R. Miranda, “Molecular Self-Assembly at Solid Surfaces,” *Advanced Materials*, vol. 23, no. 44, pp. 5148–5176, Nov. 2011, doi: 10.1002/adma.201102022.

[28] K. Xu *et al.*, “On-Surface Synthesis of a Nonplanar Porous Nanographene,” *J Am Chem Soc*, vol. 141, no. 19, pp. 7726–7730, May 2019, doi: 10.1021/jacs.9b03554.

[29] J. Zhou *et al.*, “2DMatPedia, an open computational database of two-dimensional materials from top-down and bottom-up approaches,” *Sci Data*, vol. 6, no. 1, Dec. 2019, doi: 10.1038/s41597-019-0097-3.

[30] “2Dmatpedia.” Accessed: Sep. 12, 2023. [Online]. Available: http://www.2dmatpedia.org/

[31] K. S. Novoselov, A. Mishchenko, A. Carvalho, and A. H. Castro Neto, “2D materials and van der Waals heterostructures,” *Science (1979)*, vol. 353, no. 6298, Jul. 2016, doi: 10.1126/science.aac9439.

[32] I. Meric *et al.*, “Graphene field-effect transistors based on boron-nitride dielectrics,” *Proceedings of the IEEE*, vol. 101, no. 7, pp. 1609–1619, 2013, doi: 10.1109/JPROC.2013.2257634.

[33] K. F. Mak, C. Lee, J. Hone, J. Shan, and T. F. Heinz, “Atomically thin MoS2: A new direct-gap semiconductor,” *Phys Rev Lett*, vol. 105, no. 13, Sep. 2010, doi: 10.1103/PhysRevLett.105.136805.

[34] M. Naguib *et al.*, “Two-Dimensional Nanocrystals Produced by Exfoliation of Ti3AlC2,” *Advanced Materials*, vol. 23, no. 37, pp. 4248–4253, Oct. 2011, doi: 10.1002/adma.201102306.

[35] R. Ma *et al.*, “$\text{Ti}_3\text{C}_2\text{T}_x$ MXene for electrode materials of supercapacitors,” *J Mater Chem A Mater*, vol. 9, no. 19, pp. 11501–11529, 2021, doi: 10.1039/D1TA00681A.

[36] Y. Wang and Y. Wang, “Recent progress in MXene layers materials for supercapacitors: High-performance electrodes,” *SmartMat*, vol. 4, no. 1, Feb. 2023, doi: 10.1002/smm2.1130.

[37] C. Li *et al.*, “High-Temperature Supercapacitors Based on MXene with Ultrahigh Volumetric Capacitance,” *ACS Mater Lett*, vol. 5, no. 8, pp. 2084–2095, Aug. 2023, doi: 10.1021/acsmaterialslett.3c00223.

[38] A. El Ghazaly *et al.*, “Enhanced supercapacitive performance of Mo1.33C MXene based asymmetric supercapacitors in lithium chloride electrolyte,” *Energy Storage Mater*, vol. 41, pp. 203–208, Oct. 2021, doi: 10.1016/j.ensm.2021.05.006.

[39] C. Wang, Z. Pan, H. Chen, X. Pu, and Z. Chen, “MXene-Based Materials for Multivalent Metal-Ion Batteries,” *Batteries*, vol. 9, no. 3, p. 174, Mar. 2023, doi: 10.3390/batteries9030174.

[40] S. Liu, Z. Song, X. Jin, R. Mao, T. Zhang, and F. Hu, “MXenes for metal-ion and metal-sulfur batteries: Synthesis, properties, and electrochemistry,” *Materials Reports: Energy*, vol. 2, no. 1, p. 100077, Feb. 2022, doi: 10.1016/j.matre.2021.100077.

[41] M. Greaves, S. Barg, and M. A. Bissett, “MXene-Based Anodes for Metal-Ion Batteries,” *Batter Supercaps*, vol. 3, no. 3, pp. 214–235, Mar. 2020, doi: 10.1002/batt.201900165.

[42] P. Das and Z. S. Wu, “MXene for energy storage: Present status and future perspectives,” *JPhys Energy*, vol. 2, no. 3. IOP Publishing Ltd, Jul. 01, 2020. doi: 10.1088/2515-7655/ab9b1d.

[43] R. Drummond, C. Huang, P. S. Grant, and S. R. Duncan, "Overcoming diffusion limitations in supercapacitors using layered electrodes," *J Power Sources*, vol. 433, p. 126579, Sep. 2019, doi: 10.1016/j.jpowsour.2019.04.107.

[44] N. Liu, R. Chen, and Q. Wan, "Recent advances in electric-double-layer transistors for bio-chemical sensing applications," *Sensors (Switzerland)*, vol. 19, no. 15. MDPI AG, Aug. 01, 2019. doi: 10.3390/s19153425.

[45] B. E. Conway, *Electrochemical Supercapacitors: Scientific Fundamentals and Technological Applications*. New York (NY): Kluwer Academic/Plenum Publishers, 1999.

[46] M. Beidaghi and Y. Gogotsi, "Capacitive energy storage in micro-scale devices: Recent advances in design and fabrication of micro-supercapacitors," *Energy Environ Sci*, vol. 7, no. 3, pp. 867–884, 2014, doi: 10.1039/c3ee43526a.

[47] K. Grigoras, J. Keskinen, L. Grönberg, J. Ahopelto, and M. Prunnila, "(Invited) Porous Silicon for Energy Storage at Microscale: Supercapacitors," *ECS Trans*, vol. 75, no. 1, pp. 97–104, Aug. 2016, doi: 10.1149/07501.0097ecst.

[48] "GCD example plot." Accessed: Nov. 16, 2023. [Online]. Available: www.ch.cam.ac.uk/group/forse

[49] D. V. Ragone, "Review of Battery Systems for Electrically Powered Vehicles," SAE Technical Paper 680453, Feb. 1968. doi: 10.4271/680453.

[50] T. Christen and M. W. Carlen, "Theory of Ragone plots," *J Power Sources*, vol. 91, no. 2, pp. 210–216, Dec. 2000, doi: 10.1016/S0378-7753(00)00474-2.

[51] A. Velasco *et al.*, "Recent trends in graphene supercapacitors: From large area to microsupercapacitors," *Sustain Energy Fuels*, vol. 5, no. 5, pp. 1235–1254, 2021, doi: 10.1039/d0se01849j.

[52] M. F. El-Kady, V. Strong, S. Dubin, and R. B. Kaner, "Laser scribing of high-performance and flexible graphene-based electrochemical capacitors," *Science (1979)*, vol. 335, no. 6074, pp. 1326–1330, 2012, doi: 10.1126/science.1216744.

[53] J. Lin *et al.*, "Laser-induced porous graphene films from commercial polymers," *Nat Commun*, vol. 5, pp. 1–8, 2014, doi: 10.1038/ncomms6714.

[54] A. Muzaffar, M. B. Ahamed, K. Deshmukh, and J. Thirumalai, "A review on recent advances in hybrid supercapacitors: Design, fabrication and applications," *Renewable and Sustainable Energy Reviews*, vol. 101, pp. 123–145, Mar. 2019, doi: 10.1016/j.rser.2018.10.026.

[55] D. P. Chatterjee and A. K. Nandi, "A review on the recent advances in hybrid supercapacitors," *J Mater Chem A Mater*, vol. 9, no. 29, pp. 15880–15918, 2021, doi: 10.1039/D1TA02505H.

[56] B. Pal, S. Yang, S. Ramesh, V. Thangadurai, and R. Jose, "Electrolyte selection for supercapacitive devices: A critical review," *Nanoscale Adv*, vol. 1, no. 10, pp. 3807–3835, 2019, doi: 10.1039/c9na00374f.

[57] Y. Gogotsi and R. M. Penner, "Energy Storage in Nanomaterials - Capacitive, Pseudocapacitive, or Battery-like?," *ACS Nano*, vol. 12, no. 3, pp. 2081–2083, 2018, doi: 10.1021/acsnano.8b01914.

[58] M. D. Stoller, S. Park, Z. Yanwu, J. An, and R. S. Ruoff, "Graphene-Based ultracapacitors," *Nano Lett*, vol. 8, no. 10, pp. 3498–3502, 2008, doi: 10.1021/nl802558y.

[59] Z. Wang *et al.*, "A novel 3D porous graphene foam prepared by chemical vapor deposition using nickel nanoparticles: Electrochemical determination of levodopa in the presence of uric acid," *Microchemical Journal*, vol. 147, pp. 163–169, Jun. 2019, doi: 10.1016/j.microc.2019.02.067.

[60] S. Drieschner *et al.*, "High surface area graphene foams by chemical vapor deposition," *2d Mater*, vol. 3, no. 4, pp. 1–18, 2016, doi: 10.1088/2053-1583/3/4/045013.

[61] M. J. Madito *et al.*, "Nickel-copper graphene foam prepared by atmospheric pressure chemical vapour deposition for supercapacitor applications," *Surf Coat Technol*, vol. 383, p. 125230, Feb. 2020, doi: 10.1016/j.surfcoat.2019.125230.

[62] W. Li, M. C. Tekell, C. Liu, J. A. Hethcock, and D. Fan, "Flexible All-Solid-State Supercapacitors of High Areal Capacitance Enabled by Porous Graphite Foams with Diverging Microtubes," *Adv Funct Mater*, vol. 28, no. 29, p. 1800601, Jul. 2018, doi: 10.1002/adfm.201800601.

[63] X. Xu *et al.*, "Three Dimensionally Free-Formable Graphene Foam with Designed Structures for Energy and Environmental Applications," *ACS Nano*, vol. 14, no. 1, pp. 937–947, Jan. 2020, doi: 10.1021/acsnano.9b08191.

[64] R. Liang *et al.*, "Transition Metal Oxide Electrode Materials for Supercapacitors: A Review of Recent Developments," *Nanomaterials*, vol. 11, no. 5, p. 1248, May 2021, doi: 10.3390/nano11051248.

[65] N. S. George, L. Maria Jose, and A. Aravind, “Review on Transition Metal Oxides and Their Composites for Energy Storage Application,” in *Updates on Supercapacitors*, IntechOpen, 2023. doi: 10.5772/intechopen.108781.

[66] G. A. Snook, P. Kao, and A. S. Best, “Conducting-polymer-based supercapacitor devices and electrodes,” *J Power Sources*, vol. 196, no. 1, pp. 1–12, Jan. 2011, doi: 10.1016/j.jpowsour.2010.06.084.

[67] Q. Meng, K. Cai, Y. Chen, and L. Chen, “Research progress on conducting polymer based supercapacitor electrode materials,” *Nano Energy*, vol. 36, pp. 268–285, Jun. 2017, doi: 10.1016/j.nanoen.2017.04.040.

[68] F. Shi, L. Li, X. Wang, C. Gu, and J. Tu, “Metal oxide/hydroxide-based materials for supercapacitors,” *RSC Adv.*, vol. 4, no. 79, pp. 41910–41921, Aug. 2014, doi: 10.1039/C4RA06136E.

[69] T. Nguyen and M. de F. Montemor, “Metal Oxide and Hydroxide–Based Aqueous Supercapacitors: From Charge Storage Mechanisms and Functional Electrode Engineering to Need-Tailored Devices,” *Advanced Science*, vol. 6, no. 9, May 2019, doi: 10.1002/advs.201801797.

[70] T. E. Balaji, H. Tanaya Das, and T. Maiyalagan, “Recent Trends in Bimetallic Oxides and Their Composites as Electrode Materials for Supercapacitor Applications,” *ChemElectroChem*, vol. 8, no. 10, pp. 1723–1746, May 2021, doi: 10.1002/celc.202100098.

[71] W. Chen *et al.*, “NiCo2S4 quantum dots with high redox reactivity for hybrid supercapacitors,” *Chemical Engineering Journal*, vol. 388, p. 124109, May 2020, doi: 10.1016/j.cej.2020.124109.

[72] M. Yu *et al.*, “Mesoporous NiCo2O4 nanoneedles grown on 3D graphene-nickel foam for supercapacitor and methanol electro-oxidation,” *Electrochim Acta*, vol. 151, pp. 99–108, 2015, doi: 10.1016/j.electacta.2014.10.156.

[73] S. Sun *et al.*, “Asymmetric supercapacitors based on a NiCo2O4/three dimensional graphene composite and three dimensional graphene with high energy density,” *J Mater Chem A Mater*, vol. 4, no. 47, pp. 18646–18653, 2016, doi: 10.1039/c6ta07746c.

[74] J. Pedrós *et al.*, “Polyaniline nanofiber sponge filled graphene foam as high gravimetric and volumetric capacitance electrode,” *J Power Sources*, vol. 317, pp. 35–42, 2016, doi: 10.1016/j.jpowsour.2016.03.041.

[75] L. G. Beka, X. Li, and W. Liu, "Nickel Cobalt Sulfide core/shell structure on 3D Graphene for supercapacitor application," *Sci Rep*, vol. 7, no. 1, pp. 1–11, 2017, doi: 10.1038/s41598-017-02309-8.

[76] M. Yu, X. Li, Y. Ma, R. Liu, J. Liu, and S. Li, "Nanohoneycomb-like manganese cobalt sulfide/three dimensional graphene-nickel foam hybid electrodes for high-rate capability supercapacitors," *Appl Surf Sci*, vol. 396, pp. 1816–1824, 2017, doi: 10.1016/j.apsusc.2016.11.203.

[77] P. Miao *et al.*, "Hydrothermal growth of 3D graphene on nickel foam as a substrate of nickel-cobalt-sulfur for high-performance supercapacitors," *J Alloys Compd*, vol. 732, pp. 613–623, 2018, doi: 10.1016/j.jallcom.2017.10.243.

[78] S. J. Patil, J. H. Kim, and D. W. Lee, "Graphene-nanosheet wrapped cobalt sulphide as a binder free hybrid electrode for asymmetric solid-state supercapacitor," *J Power Sources*, vol. 342, pp. 652–665, 2017, doi: 10.1016/j.jpowsour.2016.12.096.

[79] P. Geng *et al.*, "Transition Metal Sulfides Based on Graphene for Electrochemical Energy Storage," *Adv Energy Mater*, vol. 8, no. 15, pp. 1–26, 2018, doi: 10.1002/aenm.201703259.

[80] E. Kamali-Heidari, Z. L. Xu, M. H. Sohi, A. Ataie, and J. K. Kim, "Core-shell structured Ni3S2 nanorods grown on interconnected Ni-graphene foam for symmetric supercapacitors," *Electrochim Acta*, vol. 271, pp. 507–518, 2018, doi: 10.1016/j.electacta.2018.03.183.

[81] Z. Kang *et al.*, "Facile synthesis of NiCo2S4 nanowire arrays on 3D graphene foam for high-performance electrochemical capacitors application," *J Mater Sci*, vol. 53, no. 14, pp. 10292–10301, 2018, doi: 10.1007/s10853-018-2251-2.

[82] X. Cai, X. Shen, L. Ma, Z. Ji, and L. kong, "Facile synthesis of nickel–cobalt sulfide/reduced graphene oxide hybrid with enhanced capacitive performance," *RSC Adv*, vol. 5, no. 72, pp. 58777–58783, 2015, doi: 10.1039/C5RA09447J.

[83] R. Li *et al.*, "High performance Ni3S2/3D graphene/nickel foam composite electrode for supercapacitor applications," *Mater Chem Phys*, vol. 257, Jan. 2021, doi: 10.1016/j.matchemphys.2020.123769.

[84] A. M. Zardkhoshoui and S. S. H. Davarani, "Synthesis of NiGa2S4-rGO on nickel foam as advanced electrode for flexible solid-state supercapacitor with superior

energy density," *J Colloid Interface Sci*, vol. 535, pp. 195–204, Feb. 2019, doi: 10.1016/j.jcis.2018.09.100.

[85] Z. Zhang, K. Chi, F. Xiao, and S. Wang, "Advanced solid-state asymmetric supercapacitors based on 3D graphene/MnO2 and graphene/polypyrrole hybrid architectures," *J Mater Chem A Mater*, vol. 3, no. 24, pp. 12828–12835, 2015, doi: 10.1039/c5ta02685g.

[86] G. Saeed, S. Kumar, N. H. Kim, and J. H. Lee, *Fabrication of 3D graphene-CNTs/A-MoO3 hybrid film as an advance electrode material for asymmetric supercapacitor with excellent energy density and cycling life*, vol. 352. Elsevier B.V., 2018. doi: 10.1016/j.cej.2018.07.026.

[87] C. Liu, H. Liang, D. Wu, X. Lu, and Q. Wang, "Direct Semiconductor Laser Writing of Few-Layer Graphene Polyhedra Networks for Flexible Solid-State Supercapacitor," *Adv Electron Mater*, vol. 4, no. 7, pp. 1–11, 2018, doi: 10.1002/aelm.201800092.

[88] G. Li *et al.*, "Inkjet printed pseudocapacitive electrodes on laser-induced graphene for electrochemical energy storage," *Mater Today Energy*, vol. 12, pp. 155–160, 2019, doi: 10.1016/j.mtener.2019.01.005.

[89] K. Y. Kim, H. Choi, C. Van Tran, and J. Bin In, "Simultaneous densification and nitrogen doping of laser-induced graphene by duplicated pyrolysis for supercapacitor applications," *J Power Sources*, vol. 441, no. October, 2019, doi: 10.1016/j.jpowsour.2019.227199.

[90] C. Zhu *et al.*, "Direct laser writing of graphene films from a polyether ether ketone precursor," *J Mater Sci*, vol. 54, no. 5, pp. 4192–4201, 2019, doi: 10.1007/s10853-018-3123-5.

[91] J. Bin In *et al.*, "Facile fabrication of flexible all solid-state micro-supercapacitor by direct laser writing of porous carbon in polyimide," *Carbon N Y*, vol. 83, pp. 144–151, Mar. 2015, doi: 10.1016/j.carbon.2014.11.017.

[92] A. Lamberti, F. Clerici, M. Fontana, and L. Scaltrito, "A highly stretchable supercapacitor using laser-induced graphene electrodes onto elastomeric substrate," *Adv Energy Mater*, vol. 6, no. 10, pp. 1–6, 2016, doi: 10.1002/aenm.201600050.

[93] R. Ye *et al.*, "Laser-Induced Graphene Formation on Wood," *Advanced Materials*, vol. 29, no. 37, p. 1702211, Oct. 2017, doi: 10.1002/adma.201702211.

[94] Z. Zhang, M. Song, J. Hao, K. Wu, C. Li, and C. Hu, “Visible light laser-induced graphene from phenolic resin: A new approach for directly writing graphene-based electrochemical devices on various substrates,” *Carbon N Y*, vol. 127, pp. 287–296, 2018, doi: 10.1016/j.carbon.2017.11.014.

[95] W. Zhang, Y. Lei, F. Ming, Q. Jiang, P. M. F. J. Costa, and H. N. Alshareef, “Lignin Laser Lithography: A Direct-Write Method for Fabricating 3D Graphene Electrodes for Microsupercapacitors,” *Adv Energy Mater*, vol. 8, no. 27, pp. 1–9, 2018, doi: 10.1002/aenm.201801840.

[96] W. Zhang, Y. Lei, Q. Jiang, F. Ming, P. M. F. J. Costa, and H. N. Alshareef, “3D Laser Scribed Graphene Derived from Carbon Nanospheres: An Ultrahigh-Power Electrode for Supercapacitors,” *Small Methods*, vol. 3, no. 5, p. 1900005, May 2019, doi: 10.1002/smtd.201900005.

[97] A. Borenstein *et al.*, “Laser-reduced graphene-oxide/ferrocene: a 3-D redox-active composite for supercapacitor electrodes,” *J Mater Chem A Mater*, vol. 6, no. 41, pp. 20463–20472, 2018, doi: 10.1039/C8TA08249A.

[98] E. Ghoniem, S. Mori, and A. Abdel-Moniem, “Low-cost flexible supercapacitors based on laser reduced graphene oxide supported on polyethylene terephthalate substrate,” *J Power Sources*, vol. 324, pp. 272–281, Aug. 2016, doi: 10.1016/j.jpowsour.2016.05.069.

[99] W. Song *et al.*, “Flexible, Stretchable, and Transparent Planar Microsupercapacitors Based on 3D Porous Laser-Induced Graphene,” *Small*, vol. 14, no. 1, p. 1702249, Jan. 2018, doi: 10.1002/smll.201702249.

[100] E.-C. Cho *et al.*, “PEDOT-modified laser-scribed graphene films as bginder– and metallic current collector–free electrodes for large-sized supercapacitors,” *Appl Surf Sci*, vol. 518, p. 146193, Jul. 2020, doi: 10.1016/j.apsusc.2020.146193.

[101] D. Bhattacharjya, C. H. Kim, J. H. Kim, I. K. You, J. Bin In, and S. M. Lee, “Fast and controllable reduction of graphene oxide by low-cost CO 2 laser for supercapacitor application,” *Appl Surf Sci*, vol. 462, no. August, pp. 353–361, 2018, doi: 10.1016/j.apsusc.2018.08.089.

[102] T. X. Tran *et al.*, “Laser-Induced Reduction of Graphene Oxide by Intensity-Modulated Line Beam for Supercapacitor Applications,” *ACS Appl Mater Interfaces*, vol. 10, no. 46, pp. 39777–39784, 2018, doi: 10.1021/acsami.8b14678.

[103] M. Parmeggiani *et al.*, “PDMS/Polyimide Composite as an Elastomeric Substrate for Multifunctional Laser-Induced Graphene Electrodes,” *ACS Appl Mater*

Interfaces, vol. 11, no. 36, pp. 33221–33230, Sep. 2019, doi: 10.1021/acsami.9b10408.

[104] F. Mahmood, H. Zhang, J. Lin, and C. Wan, "Laser-Induced Graphene Derived from Kraft Lignin for Flexible Supercapacitors," *ACS Omega*, vol. 5, no. 24, pp. 14611–14618, Jun. 2020, doi: 10.1021/acsomega.0c01293.

[105] R. Kumar *et al.*, "Fabrication of interdigitated micro-supercapacitor devices by direct laser writing onto ultra-thin, flexible and free-standing graphite oxide films," *RSC Adv*, vol. 6, no. 88, pp. 84769–84776, 2016, doi: 10.1039/C6RA17516C.

[106] R. Kumar *et al.*, "Direct laser writing of micro-supercapacitors on thick graphite oxide films and their electrochemical properties in different liquid inorganic electrolytes," *J Colloid Interface Sci*, vol. 507, pp. 271–278, Dec. 2017, doi: 10.1016/j.jcis.2017.08.005.

[107] S. M. B. Malek Hosseini, S. M. Baizaee, H. R. Naderi, and A. Dare Kordi, "Excimer laser assisted very fast exfoliation and reduction of graphite oxide at room temperature under air ambient for Supercapacitors electrode," *Appl Surf Sci*, vol. 427, pp. 507–516, 2018, doi: 10.1016/j.apsusc.2017.08.029.

[108] B. Xie *et al.*, "Laser-processed graphene based micro-supercapacitors for ultrathin, rollable, compact and designable energy storage components," *Nano Energy*, vol. 26, pp. 276–285, Aug. 2016, doi: 10.1016/j.nanoen.2016.04.045.

[109] R. Kumar *et al.*, "Fabrication and electrochemical evaluation of micro-supercapacitors prepared by direct laser writing on free-standing graphite oxide paper," *Energy*, vol. 179, pp. 676–684, Jul. 2019, doi: 10.1016/j.energy.2019.05.032.

[110] X. Mao *et al.*, "The preparation and characteristic of poly (3,4-ethylenedioxythiophene)/reduced graphene oxide nanocomposite and its application for supercapacitor electrode," *Materials Science and Engineering: B*, vol. 216, pp. 16–22, Feb. 2017, doi: 10.1016/j.mseb.2016.10.002.

[111] G. Li, X. Mo, W.-C. Law, and K. C. Chan, "3D printed graphene/nickel electrodes for high areal capacitance electrochemical storage," *J Mater Chem A Mater*, vol. 7, no. 8, pp. 4055–4062, 2019, doi: 10.1039/C8TA11121A.

[112] F. Wang *et al.*, "Laser-induced nitrogen-doped hierarchically porous graphene for advanced electrochemical energy storage," *Carbon N Y*, vol. 150, pp. 396–407, Sep. 2019, doi: 10.1016/j.carbon.2019.05.037.

[113] K. Gholami Laelabadi, R. Moradian, and I. Manouchehri, "One-Step Fabrication of Flexible, Cost/Time Effective, and High Energy Storage Reduced Graphene Oxide@PANI Supercapacitor," *ACS Appl Energy Mater*, vol. 3, no. 6, pp. 5301–5312, Jun. 2020, doi: 10.1021/acsaem.0c00317.

[114] A. Ladrón-de-Guevara *et al.*, "Reduced graphene oxide/polyaniline electrochemical supercapacitors fabricated by laser," *Appl Surf Sci*, vol. 467–468, no. June 2018, pp. 691–697, 2019, doi: 10.1016/j.apsusc.2018.10.194.

[115] S. Yang, Y. Li, J. Sun, and B. Cao, "Laser induced oxygen-deficient TiO2/graphene hybrid for high-performance supercapacitor," *J Power Sources*, vol. 431, no. May, pp. 220–225, 2019, doi: 10.1016/j.jpowsour.2019.05.016.

[116] F. Clerici *et al.*, "In situ MoS2 Decoration of Laser-Induced Graphene as Flexible Supercapacitor Electrodes," *ACS Appl Mater Interfaces*, vol. 8, no. 16, pp. 10459–10465, 2016, doi: 10.1021/acsami.6b00808.

[117] S. M. Lee, Y. J. Park, and J. H. Kim, "Laser Reduction of Zn-Infiltrated Multilayered Graphene Oxide as Electrode Materials for Supercapacitors," *ACS Appl Nano Mater*, vol. 2, no. 6, pp. 3711–3717, 2019, doi: 10.1021/acsanm.9b00618.

[118] Y. Shao, J. Li, Y. Li, H. Wang, Q. Zhang, and R. B. Kaner, "Flexible quasi-solid-state planar micro-supercapacitor based on cellular graphene films," *Mater Horiz*, vol. 4, no. 6, pp. 1145–1150, 2017, doi: 10.1039/c7mh00441a.

[119] Y. Yue *et al.*, "Highly Self-Healable 3D Microsupercapacitor with MXene-Graphene Composite Aerogel," *ACS Nano*, vol. 12, no. 5, pp. 4224–4232, 2018, doi: 10.1021/acsnano.7b07528.

[120] J. Yoo, S. Byun, C. W. Lee, C. Y. Yoo, and J. Yu, "Precisely geometry controlled microsupercapacitors for ultrahigh areal capacitance, volumetric capacitance, and energy density," *Chemistry of Materials*, vol. 30, no. 12, pp. 3979–3990, 2018, doi: 10.1021/acs.chemmater.7b03786.

[121] J. Ye *et al.*, "Direct Laser Writing of Graphene Made from Chemical Vapor Deposition for Flexible, Integratable Micro-Supercapacitors with Ultrahigh Power Output," *Advanced Materials*, vol. 30, no. 27, pp. 1–8, 2018, doi: 10.1002/adma.201801384.

[122] T. Purkait, G. Singh, N. Kamboj, M. Das, and R. S. Dey, "All-porous heterostructure of reduced graphene oxide-polypyrrole-nanoporous gold for a planar flexible supercapacitor showing outstanding volumetric capacitance and

energy density," *J Mater Chem A Mater*, vol. 6, no. 45, pp. 22858–22869, 2018, doi: 10.1039/c8ta07627h.

[123] J. Gao *et al.*, "Laser-Assisted Multiscale Fabrication of Configuration-Editable Supercapacitors with High Energy Density," *ACS Nano*, vol. 13, no. 7, pp. 7463–7470, 2019, doi: 10.1021/acsnano.9b02176.

[124] T. Wang *et al.*, "3D-printed interdigitated graphene framework as superior support of metal oxide nanostructures for remarkable micro-pseudocapacitors," *Electrochim Acta*, vol. 319, pp. 245–252, 2019, doi: 10.1016/j.electacta.2019.06.163.

[125] F. Zhou *et al.*, "Electrochemically Scalable Production of Fluorine-Modified Graphene for Flexible and High-Energy Ionogel-Based Microsupercapacitors," *J Am Chem Soc*, vol. 140, no. 26, pp. 8198–8205, 2018, doi: 10.1021/jacs.8b03235.

[126] C. Couly *et al.*, "Asymmetric Flexible MXene-Reduced Graphene Oxide Micro-Supercapacitor," *Adv Electron Mater*, vol. 4, no. 1, pp. 1–8, 2018, doi: 10.1002/aelm.201700339.

[127] H. Xiao *et al.*, "Stretchable tandem micro-supercapacitors with high voltage output and exceptional mechanical robustness," *Energy Storage Mater*, vol. 13, no. November 2017, pp. 233–240, 2018, doi: 10.1016/j.ensm.2018.01.019.

[128] J. Qin *et al.*, "Hierarchical Ordered Dual-Mesoporous Polypyrrole/Graphene Nanosheets as Bi-Functional Active Materials for High-Performance Planar Integrated System of Micro-Supercapacitor and Gas Sensor," *Adv Funct Mater*, vol. 30, no. 16, pp. 1–9, 2020, doi: 10.1002/adfm.201909756.

[129] X. Shi *et al.*, "Ultrahigh-voltage integrated micro-supercapacitors with designable shapes and superior flexibility," *Energy Environ Sci*, vol. 12, no. 5, pp. 1534–1541, 2019, doi: 10.1039/c8ee02924e.

[130] J. K. Chih, A. Jamaluddin, F. Chen, J. K. Chang, and C. Y. Su, "High energy density of all-screen-printable solid-state microsupercapacitors integrated by graphene/CNTs as hierarchical electrodes," *J Mater Chem A Mater*, vol. 7, no. 20, pp. 12779–12789, 2019, doi: 10.1039/c9ta01460h.

[131] Y. Liu *et al.*, "Development of Graphene Oxide/Polyaniline Inks for High Performance Flexible Microsupercapacitors via Extrusion Printing," *Adv Funct Mater*, vol. 28, no. 21, 2018, doi: 10.1002/adfm.201706592.

[132] R. Agrawal and C. Wang, "On-chip asymmetric microsupercapacitors combining reduced graphene oxide and manganese oxide for high energy-

power tradeoff," *Micromachines (Basel)*, vol. 9, no. 8, 2018, doi: 10.3390/mi9080399.

[133] L. Naderi, S. Shahrokhian, and F. Soavi, "Fabrication of a 2.8 v high-performance aqueous flexible fiber-shaped asymmetric micro-supercapacitor based on MnO2/PEDOT:PSS-reduced graphene oxide nanocomposite grown on carbon fiber electrode," *J Mater Chem A Mater*, vol. 8, no. 37, pp. 19588–19602, 2020, doi: 10.1039/d0ta06561g.

[134] S. Sahoo, G. Sahoo, S. M. Jeong, and C. S. Rout, "A review on supercapacitors based on plasma enhanced chemical vapor deposited vertical graphene arrays," *J Energy Storage*, vol. 53, p. 105212, Sep. 2022, doi: 10.1016/j.est.2022.105212.

[135] A. Vyas *et al.*, "Investigation of palladium current collectors for vertical graphene-based microsupercapacitors," *J Phys Conf Ser*, vol. 1319, no. 1, p. 012007, Sep. 2019, doi: 10.1088/1742-6596/1319/1/012007.

[136] A. Velasco *et al.*, "Investigation of vertical carbon nanosheet growth and its potential for microsupercapacitors," *J Phys Conf Ser*, vol. 1837, no. 1, p. 012006, Mar. 2021, doi: 10.1088/1742-6596/1837/1/012006.

[137] J. Lin *et al.*, "3-Dimensional Graphene Carbon Nanotube Carpet-Based Microsupercapacitors With High Electrochemical Performance," *Nano Lett*, vol. 13, no. 1, pp. 72–78, 2013, doi: 10.1021/nl3034976.

[138] A. Tiliakos, A. M. I. Trefilov, E. Tanasă, A. Balan, and I. Stamatin, "Space-Filling Supercapacitor Carpets: Highly scalable fractal architecture for energy storage," *J Power Sources*, vol. 384, pp. 145–155, 2018, doi: 10.1016/j.jpowsour.2018.02.061.

[139] H. Wu, W. Zhang, S. Kandambeth, O. Shekhah, M. Eddaoudi, and H. N. Alshareef, "Conductive Metal–Organic Frameworks Selectively Grown on Laser-Scribed Graphene for Electrochemical Microsupercapacitors," *Adv Energy Mater*, vol. 9, no. 21, pp. 1–8, 2019, doi: 10.1002/aenm.201900482.

[140] G. Bhattacharya, S. J. Fishlock, A. Pritam, S. Sinha Roy, and J. A. McLaughlin, "Recycled Red Mud–Decorated Porous 3D Graphene for High-Energy Flexible Micro-Supercapacitor," *Adv Sustain Syst*, vol. 4, no. 4, pp. 1–9, 2020, doi: 10.1002/adsu.201900133.

[141] X. Yu *et al.*, "Ultra-thick 3D graphene frameworks with hierarchical pores for high-performance flexible micro-supercapacitors," *J Power Sources*, vol. 478, no. October, p. 229075, 2020, doi: 10.1016/j.jpowsour.2020.229075.

[142] C. Zhu, X. Dong, X. Mei, M. Gao, K. Wang, and D. Zhao, “Direct laser writing of MnO2 decorated graphene as flexible supercapacitor electrodes,” *J Mater Sci*, vol. 55, no. 36, pp. 17108–17119, 2020, doi: 10.1007/s10853-020-05212-2.

[143] H. Liu *et al.*, “Laser-oxidized Fe3O4 nanoparticles anchored on 3D macroporous graphene flexible electrodes for ultrahigh-energy in-plane hybrid micro-supercapacitors,” *Nano Energy*, vol. 77, no. May, p. 105058, 2020, doi: 10.1016/j.nanoen.2020.105058.

[144] R. Xu, P. Liu, G. Ji, L. Gao, and J. Zhao, “Versatile strategy to design flexible planar-integrated microsupercapacitors based on Co3O4-decorated laser-induced graphene,” *ACS Appl Energy Mater*, vol. 3, no. 11, pp. 10676–10684, 2020, doi: 10.1021/acsaem.0c01744.

[145] C. Kim, D. Y. Kang, and J. H. Moon, “Full lithographic fabrication of boron-doped 3D porous carbon patterns for high volumetric energy density microsupercapacitors,” *Nano Energy*, vol. 53, pp. 182–188, 2018, doi: 10.1016/j.nanoen.2018.08.044.

[146] P. Simon and Y. Gogotsi, “Perspectives for electrochemical capacitors and related devices,” *Nat Mater*, vol. 19, no. 11, pp. 1151–1163, Nov. 2020, doi: 10.1038/s41563-020-0747-z.

[147] T. S. Mathis, N. Kurra, X. Wang, D. Pinto, P. Simon, and Y. Gogotsi, “Energy Storage Data Reporting in Perspective—Guidelines for Interpreting the Performance of Electrochemical Energy Storage Systems,” *Adv Energy Mater*, vol. 9, no. 39, Oct. 2019, doi: 10.1002/aenm.201902007.

[148] S. Oukassi *et al.*, “Millimeter scale thin film batteries for integrated high energy density storage,” in *2019 IEEE International Electron Devices Meeting (IEDM)*, 2019, pp. 26.1.1-26.1.4. doi: 10.1109/IEDM19573.2019.8993483.

[149] “NREL best research-cell efficiencies.” Accessed: Sep. 11, 2023. [Online]. Available: https://www.nrel.gov/pv/assets/pdfs/best-research-cell-efficiencies.pdf

[150] G. Zhang *et al.*, “Renewed Prospects for Organic Photovoltaics,” *Chem Rev*, vol. 122, no. 18, pp. 14180–14274, Sep. 2022, doi: 10.1021/acs.chemrev.1c00955.

[151] S. Das, D. Pandey, J. Thomas, and T. Roy, “The Role of Graphene and Other 2D Materials in Solar Photovoltaics,” *Advanced Materials*, vol. 31, no. 1, Jan. 2019, doi: 10.1002/adma.201802722.

[152] J. Y. Kim, J.-W. Lee, H. S. Jung, H. Shin, and N.-G. Park, "High-Efficiency Perovskite Solar Cells," *Chem Rev*, vol. 120, no. 15, pp. 7867–7918, Aug. 2020, doi: 10.1021/acs.chemrev.0c00107.

[153] A. Kasry, M. A. Kuroda, G. J. Martyna, G. S. Tulevski, and A. A. Bol, "Chemical Doping of Large-Area Stacked Graphene Films for Use as Transparent, Conducting Electrodes," *ACS Nano*, vol. 4, no. 7, pp. 3839–3844, Jul. 2010, doi: 10.1021/nn100508g.

[154] X. Li *et al.*, "Graphene-On-Silicon Schottky Junction Solar Cells," *Advanced Materials*, vol. 22, no. 25, pp. 2743–2748, Jul. 2010, doi: 10.1002/adma.200904383.

[155] M. Zhao *et al.*, "Advances in Two-Dimensional Materials for Optoelectronics Applications," *Crystals (Basel)*, vol. 12, no. 8, p. 1087, Aug. 2022, doi: 10.3390/cryst12081087.

[156] O. Leenaerts, B. Partoens, F. M. Peeters, A. Volodin, and C. Van Haesendonck, "The work function of few-layer graphene," *Journal of Physics: Condensed Matter*, vol. 29, no. 3, p. 035003, Jan. 2017, doi: 10.1088/0953-8984/29/3/035003.

[157] X. Li *et al.*, "Ion doping of graphene for high-efficiency heterojunction solar cells," *Nanoscale*, vol. 5, no. 5, pp. 1945–1948, Feb. 2013, doi: 10.1039/C2NR33795A.

[158] T. Cui *et al.*, "Enhanced efficiency of graphene/silicon heterojunction solar cells by molecular doping," *J Mater Chem A Mater*, vol. 1, no. 18, pp. 5736–5740, Apr. 2013, doi: 10.1039/C3TA01634J.

[159] X. Miao *et al.*, "High Efficiency Graphene Solar Cells by Chemical Doping," *Nano Lett*, vol. 12, no. 6, pp. 2745–2750, Jun. 2012, doi: 10.1021/nl204414u.

[160] Z. Kang *et al.*, "Self-deposition of Pt nanoparticles on graphene woven fabrics for enhanced hybrid Schottky junctions and photoelectrochemical solar cells," *Physical Chemistry Chemical Physics*, vol. 18, no. 3, pp. 1992–1997, 2016, doi: 10.1039/C5CP06893B.

[161] T. Feng *et al.*, "Efficiency enhancement of graphene/silicon-pillar-array solar cells by HNO3 and PEDOT-PSS," *Nanoscale*, vol. 4, no. 6, p. 2130, 2012, doi: 10.1039/c2nr12001a.

[162] J.-K. Chang, C.-C. Hsu, S.-Y. Liu, C.-I. Wu, M. Gharib, and N.-C. Yeh, "Spectroscopic studies of the physical origin of environmental aging effects on doped graphene," *J Appl Phys*, vol. 119, no. 23, Jun. 2016, doi: 10.1063/1.4953815.

[163] Y. F. Li *et al.*, “Schottky junction solar cells based on graphene with different numbers of layers,” *Appl Phys Lett*, vol. 104, no. 4, Jan. 2014, doi: 10.1063/1.4863683.

[164] E. Shi *et al.*, “TiO2-coated carbon nanotube-silicon solar cells with efficiency of 15%,” *Sci Rep*, vol. 2, 2012, doi: 10.1038/srep00884.

[165] X. Gan *et al.*, “Polymer-coated graphene films as anti-reflective transparent electrodes for Schottky junction solar cells,” *J Mater Chem A Mater*, vol. 4, no. 36, pp. 13795–13802, 2016, doi: 10.1039/C6TA06261J.

[166] K. Ding *et al.*, “Hue tunable, high color saturation and high-efficiency graphene/silicon heterojunction solar cells with MgF2/ZnS double anti-reflection layer,” *Nano Energy*, vol. 46, pp. 257–265, Apr. 2018, doi: 10.1016/j.nanoen.2018.02.005.

[167] C. Xie *et al.*, “High-efficiency, air stable graphene/Si micro-hole array Schottky junction solar cells,” *J Mater Chem A Mater*, vol. 1, no. 48, p. 15348, 2013, doi: 10.1039/c3ta13750c.

[168] A. Alnuaimi, I. Almansouri, I. Saadat, and A. Nayfeh, “Interface engineering of graphene–silicon Schottky junction solar cells with an Al $_2$ O $_3$ interfacial layer grown by atomic layer deposition,” *RSC Adv*, vol. 8, no. 19, pp. 10593–10597, 2018, doi: 10.1039/C7RA13443F.

[169] J. Ma, Y. Yuan, and P. Sun, “Performances enhancement of graphene/n-Si Schottky junction solar cells with dual-functional MoS2 interfacial layers,” *J Alloys Compd*, vol. 883, p. 160898, Nov. 2021, doi: 10.1016/j.jallcom.2021.160898.

[170] A. Boscá, A. Ladrón-de-Guevara, J. Pedros, J. Martínez, R. Fandan, and F. Calle, “Parameter Space for Chemical Vapor Deposition Graphene in Cold-Wall Reactors under High Precursor Flow Rate,” *Cryst Growth Des*, vol. 23, no. 9, pp. 6349–6358, Sep. 2023, doi: 10.1021/acs.cgd.3c00258.

[171] J. Kraus, M. Böbel, and S. Günther, “Suppressing graphene nucleation during CVD on polycrystalline Cu by controlling the carbon content of the support foils,” *Carbon N Y*, vol. 96, pp. 153–165, 2016, doi: 10.1016/j.carbon.2015.09.048.

[172] B. Huet and J. P. Raskin, “Role of Cu foil in-situ annealing in controlling the size and thickness of CVD graphene domains,” *Carbon N Y*, vol. 129, pp. 270–280, 2018, doi: 10.1016/j.carbon.2017.12.043.

[173] Y. Jin *et al.*, "Roles of H2in annealing and growth times of graphene CVD synthesis over copper foil," *J Mater Chem A Mater*, vol. 2, no. 38, pp. 16208–16216, 2014, doi: 10.1039/c4ta02557a.

[174] A. Boscá, J. Pedrós, J. Martínez, T. Palacios, and F. Calle, "Automatic graphene transfer system for improved material quality and efficiency," *Nature Publishing Group*, 2016, doi: 10.1038/srep21676.

[175] A. Boscá Mojena, J. Pedros Ayala, J. Martínez Rodrigo, F. Calle Gómez, and T. Palacios Gutiérrez, "Method for transferring nanolayers and apparatus for carrying out said method," WO2015075292A1, May 28, 2015

[176] A. Velasco, Y. K. Ryu, A. Hamada, A. de Andrés, F. Calle, and J. Martinez, "Laser-Induced Graphene Microsupercapacitors: Structure, Quality, and Performance," *Nanomaterials*, vol. 13, no. 5, p. 788, Feb. 2023, doi: 10.3390/nano13050788.

[177] "Solar cell I-V curve example." Accessed: Nov. 16, 2023. [Online]. Available: pveducation.org

[178] A. Tiliakos, C. Ceaus, S. M. Iordache, E. Vasile, and I. Stamatin, "Morphic transitions of nanocarbons via laser pyrolysis of polyimide films," *J Anal Appl Pyrolysis*, vol. 121, pp. 275–286, 2016, doi: 10.1016/j.jaap.2016.08.007.

[179] M. Abdulhafez, G. N. Tomaraei, and M. Bedewy, "Fluence-Dependent Morphological Transitions in Laser-Induced Graphene Electrodes on Polyimide Substrates for Flexible Devices," *ACS Appl Nano Mater*, vol. 4, no. 3, pp. 2973–2986, 2021, doi: 10.1021/acsanm.1c00101.

[180] Z. Ni, Y. Wang, T. Yu, and Z. Shen, "Raman spectroscopy and imaging of graphene," *Nano Res*, vol. 1, no. 4, pp. 273–291, 2008, doi: 10.1007/s12274-008-8036-1.

[181] D. L. Silva *et al.*, "Raman spectroscopy analysis of number of layers in mass-produced graphene flakes," *Carbon N Y*, vol. 161, pp. 181–189, 2020, doi: 10.1016/j.carbon.2020.01.050.

[182] G. Anemone *et al.*, "Quality of graphene on sapphire: Long-range order from helium diffraction versus lattice defects from Raman spectroscopy," *RSC Adv*, vol. 6, no. 25, pp. 21235–21245, 2016, doi: 10.1039/c5ra27452d.

[183] K. Sun *et al.*, "High energy density of quasi-solid-state supercapacitor based on redox-mediated gel polymer electrolyte," *RSC Adv*, vol. 6, no. 60, pp. 55225–55232, 2016, doi: 10.1039/C6RA06797B.

[184] X. Li *et al.*, "High energy flexible supercapacitors formed via bottom-up infilling of gel electrolytes into thick porous electrodes," *Nat Commun*, vol. 9, no. 1, 2018, doi: 10.1038/s41467-018-04937-8.

[185] H. Dai *et al.*, "Polymer gel electrolytes for flexible supercapacitors: Recent progress, challenges, and perspectives," *Energy Storage Mater*, vol. 34, pp. 320–355, Jan. 2021, doi: 10.1016/J.ENSM.2020.09.018.

[186] B.-A. Mei, O. Munteshari, J. Lau, B. Dunn, and L. Pilon, "Physical Interpretations of Nyquist Plots for EDLC Electrodes and Devices," *The Journal of Physical Chemistry C*, vol. 122, no. 1, pp. 194–206, Jan. 2018, doi: 10.1021/acs.jpcc.7b10582.

[187] Z. Peng, J. Lin, R. Ye, E. L. G. Samuel, and J. M. Tour, "Flexible and stackable laser-induced graphene supercapacitors," *ACS Appl Mater Interfaces*, vol. 7, no. 5, pp. 3414–3419, 2015, doi: 10.1021/am509065d.

[188] M. Khandelwal, C. Van Tran, and J. Bin In, "Nitrogen and phosphorous Co-Doped Laser-Induced Graphene: A High-Performance electrode material for supercapacitor applications," *Appl Surf Sci*, vol. 576, no. PA, p. 151714, 2022, doi: 10.1016/j.apsusc.2021.151714.

[189] Y. Chyan, R. Ye, Y. Li, S. P. Singh, C. J. Arnusch, and J. M. Tour, "Laser-Induced Graphene by Multiple Lasing: Toward Electronics on Cloth, Paper, and Food," *ACS Nano*, vol. 12, no. 3, pp. 2176–2183, 2018, doi: 10.1021/acsnano.7b08539.

[190] Y. Li *et al.*, "Laser-Induced Graphene in Controlled Atmospheres: From Superhydrophilic to Superhydrophobic Surfaces," *Advanced Materials*, vol. 29, no. 27, 2017, doi: 10.1002/adma.201700496.

[191] L. Li *et al.*, "High-Performance Pseudocapacitive Microsupercapacitors from Laser-Induced Graphene," *Advanced Materials*, vol. 28, no. 5, pp. 838–845, 2016, doi: 10.1002/adma.201503333.

[192] M. Khandelwal, C. Van Tran, J. Lee, and J. Bin In, "Nitrogen and boron co-doped densified laser-induced graphene for supercapacitor applications," *Chemical Engineering Journal*, vol. 428, no. June 2021, p. 131119, 2021, doi: 10.1016/j.cej.2021.131119.

[193] A. K. Yagati *et al.*, “Laser-induced graphene interdigitated electrodes for label-free or nanolabel-enhanced highly sensitive capacitive aptamer-based biosensors,” *Biosens Bioelectron*, vol. 164, no. April, p. 112272, 2020, doi: 10.1016/j.bios.2020.112272.

[194] R. Barber *et al.*, “Laser induced graphene sensors for assessing pH: Application to wound management,” *Electrochem commun*, vol. 123, p. 106914, 2021, doi: 10.1016/j.elecom.2020.106914.

[195] X. Li *et al.*, “High-Voltage Flexible Microsupercapacitors Based on Laser-Induced Graphene,” *ACS Appl Mater Interfaces*, vol. 10, no. 31, pp. 26357–26364, 2018, doi: 10.1021/acsami.8b10301.

[196] W. Wang, L. Lu, Z. Li, and Y. Xie, “Laser induced 3D porous graphene dots: Bottom-up growth mechanism, multi-physics coupling effect and surface wettability,” *Appl Surf Sci*, vol. 592, no. December 2021, p. 153242, 2022, doi: 10.1016/j.apsusc.2022.153242.

[197] D. Austin *et al.*, “Laser writing of electronic circuitry in thin film molybdenum disulfide: A transformative manufacturing approach,” *Materials Today*, vol. 43, pp. 17–26, Mar. 2021, doi: 10.1016/j.mattod.2020.09.036.

[198] K. O. Oyedotun, T. M. Masikhwa, S. Lindberg, A. Matic, P. Johansson, and N. Manyala, “Comparison of ionic liquid electrolyte to aqueous electrolytes on carbon nanofibres supercapacitor electrode derived from oxygen-functionalized graphene,” *Chemical Engineering Journal*, vol. 375, p. 121906, Nov. 2019, doi: 10.1016/j.cej.2019.121906.

[199] R. R. Nair *et al.*, “Fine Structure Constant Defines Visual Transparency of Graphene,” *Science (1979)*, vol. 320, no. 5881, pp. 1308–1308, Jun. 2008, doi: 10.1126/science.1156965.

[200] K. K. Kim *et al.*, “Enhancing the conductivity of transparent graphene films via doping,” *Nanotechnology*, vol. 21, no. 28, p. 285205, Jul. 2010, doi: 10.1088/0957-4484/21/28/285205.

[201] R. Saive, “S-Shaped Current–Voltage Characteristics in Solar Cells: A Review,” *IEEE J Photovolt*, vol. 9, no. 6, pp. 1477–1484, Nov. 2019, doi: 10.1109/JPHOTOV.2019.2930409.

[202] Y. Choi, J. Lee, J. Seo, S. Jung, U. Kim, and H. Park, “The effect of the graphene integration process on the performance of graphene-based Schottky junction

solar cells," *J Mater Chem A Mater*, vol. 5, no. 35, pp. 18716–18724, 2017, doi: 10.1039/C7TA05481E.

Annexes

A. Publications

- Velasco, Y. K. Ryu, A. Boscá, A. Ladrón-de-Guevara, E. Hunt, J. Zuo, J. Pedrós, F. Calle and J. Martínez, "Recent trends in graphene supercapacitors: From large area to microsupercapacitors," Sustain Energy Fuels, vol. 5, no. 5, pp. 1235–1254, 2021.
    - Selected as front cover for volume 5, issue 5 (2021)
    - Highly cited article certificate from the Royal Society of Chemistry (top 5% in 2022)
- Velasco, Y. K. Ryu, A. Hamada, A. de Andrés, F. Calle and J. Martínez, "Laser-induced graphene microsupercapacitors: structure, quality and performance" Nanomaterials, vol. 13, no. 5, pp. 788, 2023.
- M. Belén Gómez-Mancebo, R. Fernández-Martínez, A. Ruiz-Perona, V. Rubio, P. Bastante, F. García-Pérez, F. Borlaf, M. Sánchez, A. Hamada, A. Velasco, Y. K. Ryu, F. Calle, L. J. Bonales, A. J. Quejido, J. Martínez and I. Rucandio, "Comparison of Thermal and Laser-Reduced Graphene Oxide Production for Energy Storage Applications" Nanomaterials, vol. 13, no. 8, pp 1391, 2023.
- H. Bukovska, F. García-Perez, N. Brea, L. J. Bonales, A. Velasco, M. A. Clavero, J. Martínez, A. J. Quejido, I. Rucandio and M.B. Gómez-Mancebo, "Evaluation and Optimization of Tour Method for Synthesis of Graphite Oxide with High Specific Surface Area" C, vol. 9, no. 3, pp. 65, 2023.
    - Selected as front cover of Volume 9, Issue 3 (2023)

Future prublications

- Hamada, Y. K. Ryu, A. Velasco, M. B. Gómez-Mancebo, F. Calle and J. Martinez. "Double Pass Effect on Laser Induced Graphene Microsupercapacitors" Manuscript to be submitted to Applied Surface Science. (under preparation)
- Martínez, Y. K. Ryu, S. Tarancón, E. Tejada, A. Hamada, A. Velasco and J. Martínez. "Laser Induced Graphene Strain Sensors for Body Movement Monitoring" Manuscript submitted to ACS Omega.

B. Scientific conferences

- Spanish conference of Electron Devices, CDE 2021, Sevilla (online format). Poster presentation "Towards a hybrid Graphene device for green energy".
- Spanish conference of Electron Devices, CDE 2023, Valencia. Oral presentation "Exploring recent trends in graphene supercapacitors"
- Graphene conference, 2023, Manchester, UK. Poster presentation "Laser-Induced Graphene Microsupercapacitors: exploring its structure, quality and performance"

C. Final degree projects

- Elijah L. Hunt, "Laser Induced Graphene Micro-supercapacitors: The Effectiveness of Electrolytes for Energy Storage". Master thesis for the completion of the Master in Materials Engineering (ETSICCP, UPM) directed by Dr. Javier Martínez and Andrés Velasco.
- Manuel Guillermo Altava Sanz "Diseño e implementación de un banco de medias conectado e interoperable basado en Arduino" Bachelor thesis for the completion of the "Grado en Ingeniería de Tecnologías y Servicios de la Comunicación" (ETSIT, UPM) directed by Andrés Velasco and endorsed by Dr. Alberto Boscá.

D. Research projects

- Dispositivos de Grafeno para la mejora de las energías renovables, DIGRAFEN. MINECO (in col. with CIEMAT), 2018-2020. ENE2017-88065-C2-2-R
- Graphenic and 2D materials for Solar Cells and Renewable Energy Storage Devices, REGRAP-2D. MICINN (in col. with CIEMAT), 2021-2024. PID2020-114234RB-C21
- New 2D materials: Characterization, properties and applications, NMAT-2D. CM P2018/NMT-4511 (in col. with LabCOA - IMDEA Nano, Department of Condensed Matter Physics - UAM, CSIC ICMM, FIDAMC). 2019-2023.

- Plan complementario Materiales Avanzados: 2D Materials. MICIN y CM, 2022-25.

E. Divulgation activities

- Semana de la Ciencia 2020. Presentación "El grafeno y su papel en los retos energéticos del futuro" (online).
- XI Noche Europea de los Investigadores 2020: Compromiso #UPM2030: tecnología para alcanzar los ODS. Presentación "El grafeno y su papel en los retos energéticos del futuro" (online).
- Semana de la Ciencia 2021. Actividad presencial "Masterchef Sostenible ¡Crea una fuente de energía verde gracias al grafeno!".
- XII Noche Europea de los Investigadores 2021: Tecnología en acción para un mundo más verde y sostenible. Actividad presencial "Masterchef Sostenible ¡Crea una fuente de energía verde gracias al grafeno!".
- Día Internacional de la mujer y la niña en la ciencia 2022. "From Argelia to Madrid: our PhD travel discovering graphene for a sustainable world".
- XI Feria Madrid es Ciencia 2022. "Grafeno para un mundo más sostenible".
- #UPMday 2022 como parte del equipo del ISOM-UPM.
- Ateneo de Madrid, ciclo de conferencias de la Sección de Medio Ambiente, 2022. "Nanotecnología para la sociedad. Energía con grafeno: verde, eficiente y barata".
- XII Noche Europea de los Investigadores 2022: Tecnología en acción para un mundo más verde y sostenible. Actividad presencial "Masterchef Sostenible ¡Crea una fuente de energía verde gracias al grafeno!".
- Semana de la Ciencia 2022. Actividad presencial "Masterchef sostenible DELUXE: energía verde con grafeno...y ahora: flexible!".
- Noche Europea de los Investigadores 2023. "Diálogo, Kahoot y taller sobre nanotecnología y futuro: energía sostenible y estructuras cuánticas".
- Semana de la Ciencia 2023. "Diálogo, Kahoot y taller sobre nanotecnología y futuro: energía sostenible y estructuras cuánticas".